THESIS

SURFACE FLUXES OF WATER, ENERGY, AND CARBON DIOXIDE AS SIMULATED BY THE SIMPLE BIOSPHERE MODEL VERSION 3 IN THE SOUTHERN GREAT PLAINS OF NORTH AMERICA AND THEIR EFFECT ON SIMULATED BOUNDARY LAYER HYDROLOGY

Submitted by

Andrew W. Philpott

Atmospheric Science Department

In partial fulfillment of the requirements

For the Degree of Master of Science

Colorado State University

Fort Collins, Colorado

Summer 2006

ABSTRACT OF THESIS

SURFACE FLUXES OF WATER, ENERGY, AND CARBON DIOXIDE AS SIMULATED BY THE SIMPLE BIOSPHERE MODEL VERSION 3 IN THE SOUTHERN GREAT PLAINS OF NORTH AMERICA AND THEIR EFFECT ON SIMULATED BOUNDARY LAYER HYDROLOGY

Land surface energy fluxes, including sensible heat flux and latent heat flux, impact Planetary Boundary Layer thickness, energy, and water vapor as well as precipitation rates. Therefore, land surface energy fluxes are important pieces of coupled land-atmosphere modeling systems.

A land surface model, the Simple Biosphere Model (SiB3), was tested in the ARM-CART SGP region in Oklahoma and Kansas, with a particular emphasis on surface energy balance components (net radiation, ground heat flux, sensible heat flux, and latent heat flux) and on the response of latent and sensible heat to vegetation stress conditions. The model was tested both coupled to a single column of the Colorado State University General Circulation Model (CSU-GCM) and using station observed weather and downwelling radiation.

In the Single Column mode, a previous version of the Simple Biosphere model, SiB2, had suffered from extreme stress feedback loops during the summer. Excessive stomatal closure in response to heat and humidity stress dried the boundary layer and increased its temperature by reducing latent heat flux, trapping the coupled system in an unreasonably dry state until

lateral forcing rewetted the atmosphere in the fall. The upgrade from SiB2 to SiB3 removed the excessive feedback, greatly improving the summertime latent heat flux and atmospheric water vapor simulations.

SiB3 surface fluxes driven from station data generally compared well to observed Energy Balance Bowen Ratio station fluxes. However, there was a universal problem of too much direct energy flow in and out of the soil during the day and night, respectively. This is accompanied by errors in sensible and latent heat flux: low upward sensible heat fluxes by day and insufficient downward nightime latent and sensible fluxes.

The soil heat flux error was attributed to inaccuracies in both the simulation of vegetation shading of the soil and in the soil thermal conductivities and capacities, which also yielded excessive seasonal and diurnal cycles in soil temperature. Further error in model sensible and latent flux can be attributed to uncertainties in vegetation stress parameters as well as uncertainty in the satellite-derived leaf to canopy scaling parameters.

Andrew W. Philpott
Atmospheric Science Department
Colorado State University
Fort Collins, CO 80523
Summer 2006

ACKNOWLEDGEMENTS

I thank my advisor, A. Scott Denning, for guidance and suggestions along the way. I also thank my graduate committee, David A. Randall and Niall P. Hanan for reviewing this thesis.

I have many to thank in the Denning Research group at Colorado State University. I wish to especially thank Ian Baker with considerable help in learning about the SiB3 model and how to use it. I thank Kevin Schaefer for valuable help and suggestions throughout this work. Neil Suits, Sheri Conner Gausepohl put together the necessary statistical values to ingest GIMMSg NDVI data into SiB, and Kathy Corbin did the same for the SPOT NDVI data, along with converting it to easy to use 1km by 1km latitude longitude maps . Lara Prihodko offered numerous useful suggestions, particularly regarding the soil parameterization and model spinup. Connie Uliasz helped to keep me in touch with other group members and my advisor, and helped me with the format of this document.

Other people at Colorado State University also were very helpful. Niall P. Hanan from my graduate committee put together the SiB3 driver data for the AmeriFlux Tallgrass site. Mark Branson from the research group of David A. Randall put together the datasets necessary for running SiB3 in the Single Column mode of the Colorado State University GCM. Brenda Thompson from the William Cotton research group helped me with the format of this document.

From outside agencies, I thank Molly E. Brown of NASA Goddard Space

Flight Center for providing the GIMMSg NDVI data. Raymond McCord, William Hargrove, Craig Brandt, and Henriette Jager from the Oak Ridge National Laboratory put together the meteorology driver datasets for SiB3 for the Atmospheric Radiation Measurement (ARM) administered sites, as well as provided quality controlled soil water and temperature data. David Cook of Oak Ridge National Laboratory, the Energy Balance Bowen Ratio (EBBR) instrument mentor for the ARM-CART SGP site helped me select the sites for which EBBR data were reliable, and explained some measurement uncertainties. The PI in charge of the AmeriFlux Tallgrass site is Shashi Verma of the University of Nebraska at Lincoln. Joseph A. Berry of the Carnegie Institute of Washington and Stanford University provided valuable suggestions for interpreting the SiB3 flux data, and for modifying the SiB3 vegetation stress parameterizations to be more appropriate for the Southern Great Plains.

This research was funded by ...

Contents

Chapter 1

Introduction

1.1 Modeling coupled land/atmosphere systems

1.1.1 General Circulation Models

Atmospheric general circulation models (GCMs) coupled to ocean models and land surface models are designed to simulate the climate system. Applications include analysis of climate change on regional scales (Garratt 1993), investigation of the cause of observed climate phenomena (Betts et al 1996), and predicting the future global climate in response to increased atmosphereic carbon dioxide (Stainforth et al 2005). In addition, if the land surface model includes carbon dioxide fluxes, the global carbon cycle itself can be investigated with these systems (Denning et al 1996b).

There are significant interactions between the land surface and the atmosphere in the real world and in GCMs. Latent and sensible heat fluxes influence convection and precipitation by modifying the moist static energy of the Planetary Boundary Layer (PBL) (Eltahir 1998) and its equivalent potential temperature θ_e (Betts et al 1996). A higher sensible heat flux increases the entrainment of low θ_e free tropospheric air at the top of the PBL. Surface albedoes and heat flux into the soil influence the sum of sensible and latent heat flux, which serves as an upward flux of high θ_e into the PBL (Betts et al 1996).

Sellers et al 1997 reviewed land surface formulations, from the most simple Bucket Models to models that simulate the physiological regulation of carbon uptake and water loss by plant leaves. In all of these models, surface energy balance is a fundamental assumption

$$R_n = G + H + LE \tag{1.1}$$

where R_n is the net radiation **received** by the surface, G is the conductive flux of energy **downward** into the soil, H is the **upward** turbulent flux of sensible energy into the air, and LE (latent heat flux) is the **upward** turbulent transfer of water vapor into the air from a surface liquid or ice source (containing the latent energy of evaporation or sublimation). Any one of these terms may be negative, indicating a flux in the opposite direction as specified above.

Surface net radiation is comprised of three components

$$R_n = S(1-\alpha) + L_d - \epsilon\sigma T_s^4 \tag{1.2}$$

where S (downwelling solar radiation) and L_d (downwelling longwave radiation) are controlled by the atmosphere, while α (surface albedo) and $\epsilon\sigma T_s^4$ (upwelling longwave radiation) are determined by the surface.

The turbulent fluxes, sensible and latent, are derived using a potential difference - resistance model, which calculates upward flux as the vertical gradient in latent or sensible energy divided by a resistance to upward transfer. Sensible energy is proportional to temperature, while latent energy is proportional to water vapor pressure.

One part of the resistance to latent heat flux is the resistance to water vapor transfer out of the leaf stomates. In addition to being the passage way for transpiration of water vapor out of the leaf, these pores allow carbon dioxide to come in. The plant uses carbon dioxide to build its organic matter, so it essentially serves as the plant's food source. But because plants also need water, the stomates stay at a limited conductance which depends on the environmental and plant water conditions. The active regulation of stomatal conductance creates a balance between water loss and carbon intake (Hopkins 1999). In land surface models, this regulation can be estimated empirically from temperature, humidity, and soil water. But more physiological formulations have been developed to mimic the enforced balance between

carbon intake and water loss (Sellers et al 1997).

1.1.2 Excessive Stomatal Feedback

A positive feedback loop between air humidity and stomatal conductance can occur in a land surface model when coupled to an atmospheric model. Under low humidity, increased stomatal resistance can further dry the air by decreasing latent heat flux. Such feedbacks occur in real life (Collatz et al 1991). However, if the land surface model exaggerates a feedback loop, the modeled climate can grow unrealistically dry. The first version of the Simple Biosphere Model (SiB1), when coupled to the Colorado State University General Circulation Model (CSU-GCM), exhibited an extreme drying of the global climate due to excessive feedback using the empirical stomatal conductance parameterization. Randall et al 1996 referred to this disaster in the simulated climate as stomatal suicide. They used a newer version of the model, SiB2, in the CSU-GCM, and simulated a much more realistic global climate. The transition between SiB1 and SiB2 from an empirical stomatal resistance model to a physiological one solved the problem of global stomatal suicide. However, SiB2 has still suffered from excessive stomatal feedback in some situations. For example, when SiB2 was run in Single Column mode at the ARM-CART SGP site, the late summer boundary layer became much too dry due to low latent heat flux (M.Branson, pers. comm.). In this thesis, a third version, SiB3, when coupled to a Single Column of the CSU-GCM at ARM-CART, is shown to no longer suffer from stomatal suicide in summer,

2000.

1.2 The Southern Great Plains

The Atmospheric Radiation Measurement Program's Cloud and Radiation Testbed Southern Great Plains site (ARM-CART SGP) is a several hundred kilometer by several hundred kilometer site in Oklahoma and Kansas, meant to be of the size of a typical GCM grid cell (Stokes and Schwartz 1994), (Fig. 1.1).

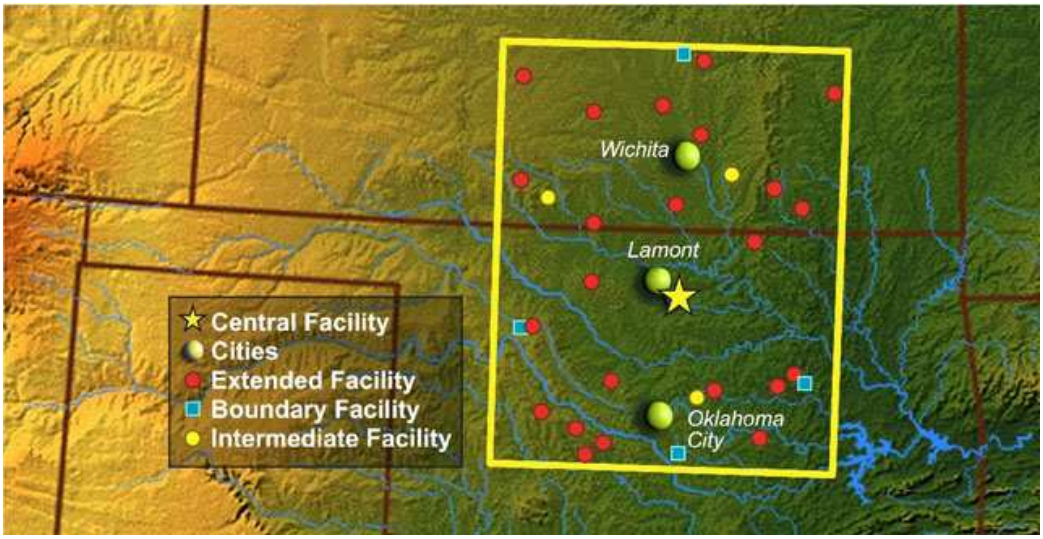

Figure 1.1: A map of the ARM-CART SGP site, courtesy of ARM.

The region has two dozen ARM administered sites that measure the surface radiation, weather, turbulent energy fluxes and soil conditions. The region also contains measurement networks administered by other agencies.

Furthermore, intensive field campaigns have been performed in the region. One of the most relevant to land surface models was the First International Satellite Land Surface Climatology Project (ISLSCP) Field Experiment (FIFE) at a 15 by 15 kilometer site in south-central Kansas (Sellers et al 1992c). Another useful set of studies involved continuous measurements centered around an Oklahoma native prairie surface flux tower administered by the University of Nebraska at Lincoln (Burba and Verma 2001, Suyker et al 2003). In this thesis, the UNL tower and eight ARM surface flux and soil measurement facilities will be compared to SiB3 simulations driven by observed weather. Whole domain ARM-CART SGP products will be used to evaluate the Single Column mode of the CSU GCM coupled to SiB3.

1.2.1 Observed Surface Conditions in the SGP region

The most important landcover classes in the ARM-CART SGP region are pasture/grassland and agriculture, primarily unirrigated winter wheat. All of the sites in this study are pasture/grassland, except that two of them have some unirrigated wheat within the likely measurement system flux footprints.

The seasonal cycle of a winter wheat field is controlled by farming practice; commonly, the vegetation increases from fall planting to early-summer harvest, after which vegetation remains sparse with very few weeds (Hanan et al 2005). As an example of the seasonal cycle of pasture and grassland, the UNL prairie site has a green leaf area index ($gLAI$) maximum in the middle to late summer. While $gLAI$ drops off quickly in the fall, substan-

tial non-photosynthtic and dead foliage remains until late March when an annual prescribed burn-off occurs. Most of the vegetation is of the C4 photosynthetic pathway in the late summer, while half of the vegetation is C3 in the cooler spring (Hanan et al 2005). No species detail is available for the other sites. However, because the C4 photosynthetic pathway is more efficient under high temperatures, C4 fraction should increase during the summer in all non-agricultural lands in and near the SGP region (Still et al 2003). Nonetheless, C4 fraction was observed to vary somewhat from location to location even over the small FIFE area (Stewart and Verma 1992). Therefore, C3 and C4 fraction should be a considerable source of uncertainty in all of the ARM site simulations.

In the FIFE and UNL grassland sites, the seasonality of LE and net carbon flux follows the seasonal cycle in green leaf area, with high latent flux and daytime carbon uptake during the summer, quickly dropping off during October (Verma et al 1992, Hanan et al 2005). Sensible flux is maximized in the early spring and the fall (Hanan et al 2005). The exception is the occasional dry spell in the later summer, where lack of soil water temporarily stresses the vegetation causing an increase in Bowen Ratio (H/LE) (Verma et al 1992) and decreased daytime carbon uptake (Suyker et al 2003).

Suyker et al 2003 showed that the green leaf area and fluxes were both highly correlated with precipitation and the amount of soil water, suggesting an ecosystem that is driven by water availability. Indeed, the shut down of a grassland in early fall occurs when temperatures are still often quite

warm. However, the vegetation remains dormant in the winter due to cold air depsite replenished of soil water.

Transpiration is often the dominant part of latent heat flux, but there are cases where the latent heat flux becomes unlinked to vegetation when there is a significant amount of direct soil evaporation. For example, after the harvest of a wheat field operated by UNL, latent heat flux remained high even after carbon uptake had shut down (Hanan et al 2005). At an irrigated Spanish field, soil evaporation was observed to increase from around 25% of total latent flux at an LAI of 3 to around 50% at an LAI of 0.7 (Villalobos and Fereres 1990).

Latent heat flux and carbon uptake show a high interannual variability at the UNL site, with water availability appearing to be a key driving force. Estimated growing season net carbon uptake decreased from $446 gC/m^2$ in 1997 to $204 gC/m^2$ in 1998, because of a drier summer 1998: less precipitation, higher 4.5 m vapor pressure defecit, and lower soil moisture (Suyker et al 2003).

During the summer, in the absense of heavy vegetation stress, LE is dominant over H and G, using 50-75% of daytime net radiation in May through August 1997 at the UNL site (Burba and Verma 2001). At a flux tower in FIFE, it used 70% of net radiation during unstressed parts of the 1987 growing season, falling to 40% during high stress periods in July (Verma et al 1992).

Daytime G downward into the soil was observed to consume roughly 15%

of net radiation at FIFE in summer 1987 (Smith et al 1992), and peaked somewhere around 10% of net radiation in early spring 1997 at the UNL site (Burba and Verma 2001). G varies considerably (by as much as 50 - 100 W/m^2) across even the small FIFE study area (Smith et al 1992, Fritschen and Qian 1992). Whether a site was grazed or not had a strong impact on G, with very little difference between sites that are burned in the spring and those that remain unburned (Smith et al 1992).

Reduced G due to vegetation shading is well documented in modeling studies (e.g. Yang et al 1999). Therefore, grazing can increase daytime G by keeping vegetation thickness low throughout the growing season. Soil texture is another important source of G variability, with soils having of higher thermal conductitivy exhibiting more energy uptake in the day and energy release at night. Two nearby soils of different texture in the ARM-CART domain exhibited significantly different daytime and nightime soil heat flows (by 50 and 25 W/m^2, respectively, yielding differences in the diurnal temperature cycle of 5-8° C) despite having very similar vegetation covers (Brotzge and Crawford 2003).

The majority of ARM-CART SGP sites exhibit a seasonal cycle of very wet soils from November through April, with drying occuring in the summer, when active transpiration removes soil water (Schneider et al 2003). Overall, the higher soil layers are more variable from site to site, and wet and dry more frequently than the lower layers, which at some sites exhibit very little seasonal cycle, remaining wet all the time.

1.2.2 Uncoupled surface model runs in the SGP region

Numerous studies of surface models driven by observed weather and radiation have been made in the SGP region. The focus here will be on tests of SiB2 with some of the upgrades that are now incorporated in SiB3: particularly two studies, one based on data from FIFE, and the other involving the UNL grassland site.

Colello et al 1998 ran three versions of SiB2 for May-September, 1987, using area averaged meteorology across the 15 by 15 kilometer FIFE domain, and comparing to a single tower's observed R_n, G, H, and LE flux data. One run, Control, used the original SiB2 model (Sellers et al 1996a,b), including the loam soil type found on the $1^\circ x 1^\circ$ global map and a 100% C4 vegetation type. Another SiB2 run, Calibrated, used a locally observed clay soil texture and a modified soil water plant stress forumulation. The third run, Tuned, used time varying C4 and C3 fractions, a three layer soil with depth dependent texture and roots in all three layers instead of only one, a further modification to soil water stress, and vegetation biophysical parameters estimated from on-site testing. Comparing the model output photosynthesis and latent heat flux rates to observations diagnosed whether the simulation had too much or too little stress. The Control run had too little soil water stress because of the high soil hydraulic conductivity of the loam. Using the locally observed clay soil in the Calibrated run improved the results, but now water stress was too high. The Tuned run produced the best results. The net radiation, soil heat flux, and sensible heat, however, were not improved

by any of the modifications. Net radiation tended to be overestimated, with a normalized standard error of 15%, while the error in G and H was on the order of 70%. In contrast, from Control to Tuned, latent heat flux normalized standard error decreased from 40% to 18% and carbon flux from 95% to 30%.

Hanan et al 2005 continued with a version of SiB2 similar to Colello et al 's Tuned run, with one additional modification: local observations of leaf area index (LAI) and fraction of photosynthetically active radiation absorbed by the canopy (fPAR) were used rather than satellite derived values. The model was run during 1997 and 1998 at the UNL prairie site and a nearby winter wheat site. We will focus on the prairie site. Daytime carbon uptake is overestimated by up to about 20% through mid-June becoming underestimated by up to 50% in July and August. The authors attribute the overestimation to errors in the leaf to canopy scaling of the photosynthesis model and late summer underestimation to lingering problems in the calculation of soil water stress. Latent heat flux shows a similar pattern to carbon uptake. A wintertime underestimation of sensible heat flux was attributed to a gross overestimation (300%, $150 W/m^2$) of ground heat flux, which improves in the summer, suggesting that ground shading by a photosynthetic canopy is better treated than that by a dormant canopy. Meanwhile, nighttime upward ground heat flux is also too large, which corresponds to a lack of dewfall and downward sensible flux in the model.

1.2.3 Single Column runs in the SGP region

As explained in Randall and Cripe 1999, single column modeling simulates only a single column of a global GCM, with the impacts of processes in neighboring areas figured from external data. They describe the purpose of a single column model (SCM) as a simplified and less computationally expensive template for testing a change in the GCM. In this thesis, a change in the land surface model is being tested.

Randall and Cripe 1999 investigate the various methods for lateral forcing. Scalar quantities within the grid cell are modified by modeled physics along the path of motion

$$\frac{Dq}{Dt} = P \tag{1.3}$$

Expanding the Lagrangian derivative, the time derivative becomes

$$\frac{\partial q}{\partial t} = -\left[u\frac{\partial q}{\partial x} + v\frac{\partial q}{\partial y} + \omega\frac{\partial q}{\partial p}\right] + P \tag{1.4}$$

In the CSU-GCM SCM, temperature and water vapor mixing ratio are the scalar variables treated.

One method (termed Revealed Forcing) prescribes the entire advective term, $\left[u\frac{\partial q}{\partial x} + v\frac{\partial q}{\partial y} + \omega\frac{\partial q}{\partial p}\right]$, from data, which allows the SCM profile of q to vary significantly from the data if P dominates. Another method (termed Relaxation Forcing) makes some significant modifications to equation 1.4, causing the modeled q profile to relax towards a data-supplied upstream q

profile on a relaxation time scale that is also prescribed from data. Randall and Cripe 1999 found that the CSU-GCM SCM profile of water vapor sometimes would become substantially drier than the incoming profile. As a result, Relaxation Forcing would force a lateral addition of water vapor, and the SCM would rain this water out to try to dry the profile out again, causing unrealistic amounts of precipitation. Such excessive precipitation inhibits evaluation of surface model performance; particularly it renders stomatal suicide impossible because the atmospheric profile is forced to conform to data, and the precipitation keeps the soil very wet. Therefore, Revealed Forcing was used to drive the SiB3-SCM system in this study.

Sud et al 2001 ran a Simplified SiB model in a single column of the Goddard Earth Observing System GEOS-2 GCM at ARM-CART, having added to SSiB a 100 layer soil hydrology model (which is analogous to SiB3's new 10 layer soil). The model was run over four periods of several weeks each. Multiple soil textures and vegetation cover fractions were tested. For the standard run, a medium soil texture and a 60% vegetation fraction, a very reasonable atmospheric profile was produced in the summer, with precipitation being 7% too low, and the lower atmosphere being 2° C too warm and having slightly too much water vapor. Certainly there was no evidence here of stomatal suicide. Some of the lack of stomatal suicide may be due to the different GCM rather than the land model, as Randall et al 1996 reported that SiB1 produced much less stomatal suicide in the Goddard GCM than in the CSU GCM. However, vegetation stress was not totally

absent, since higher vegetation fractions sometimes produced lower latent heat fluxes. In contrast to the Colello et al 1998 offline SiB2 results, finer soils exhibited more latent heat flux than the medium soil, due probably to greater water retention.

Although evaporation was significantly affected by surface type, precipitation was much less sensitive in three of the four periods. This indicates that in spite of an important surface influence on the local atmosphere, precipitation is still highly affected by the large scale flow patterns and the advection of water vapor from elsewhere.

Chapter 2

Experiment Design

2.1 SiB3 Model Design

SiB3 is built upon SiB2 (Sellers et al 1996a,b). A prognostic canopy airspace has been added (Baker et al 2003), as has the possibility of monthly varying C3 and C4 fractions within the canopy rather than only either fully C3 or C4 vegetation (Hanan et al 2005). The three soil zones of surface, root, and recharge have been replaced with a ten layer soil of increasing layer thickness with depth and roots in all layers, adapted from the Community Land Model (Dai et al 2003), and based on the earlier NCAR Land Surface Model (Bonan 1996). Also adapted from CLM, a prognostic snow cover is divided into up to 5 layers, with the number of layers dependent upon the total snow mass. Finally, there have been a number of modifications to some of the details of SiB2. For example, the soil water stress parameter has been

modified, as based on the method of Colello et al 1998.

This section describes features of SiB3 relevant to the ARM-CART simulations of soil hydrology, surface energy fluxes, and carbon assimilation. The photosynthesis-stomatal conductance submodel will be described in detail, along with a description of the soil water equations, the water and energy balance of the surface, and the use of NDVI data to derive vegetation parameters. SiB3 has additional capabilities not considered here; particularly it can simulate biosphere carbon respiration and descriminate carbon isotopes.

The model structure consists of time invariant surface parameters, time varying surface parameters, time varying upper boundary conditions, prognostic variables, and diagnostic variables (Sellers et al 1996a). Most of the time invariant parameters specify soil texture and plant biophysical quantities (Table 2.1). Time varying surface parameters are controlled by Normalized Difference Vegetation Index (NDVI) input data, and are specified once per month. The upper boundary conditions are downwelling radiation components and precipitation and mixed layer PBL values of meteorological variables (Table 2.2). In coupled mode, these upper boundary conditions are supplied by the General Circulation Model every timestep (10 minutes in the simulations herein), but by observations or model reanalysis products when SiB3 is run uncoupled (at whatever time resolution is available). In uncoupled mode, SiB3 uses a simple approximation to separate observed downwelling total shortwave radiation into four components: diffuse and di-

Table 2.1: SiB3 Time Invariant soil texture and biophysical parameters, with C3 and C4 (if different from C3) biophysical parameters appropriate for the ARM-CART region specified. The values come from the tables of Sellers et al 1996b, vegetation types C3 grassland and C4 grassland

	Soil Parameters	
b	moisture retention curve exponent	
ψ_s	saturated matric potential	
θ_s	porosity	
K_s	saturated hydraulic conductivity	

	Biophysical Parameters	**C3**	**C4**
$z2$	canopy top (m)	1.0	
$z1$	canopy bottom (m)	0.1	
σ_V	fraction of ground covered by vegetation	varies	
χ_l	leaf angle distribution factor	-0.3	
δ_{gv}	green leaf transmittance to visible	0.07	
δ_{bv}	non-green vegetation transmittance to vis	0.22	
δ_{gn}	green leaf transmittance to near-infrared	0.248	
δ_{bn}	non-green veg. transmittance to nir	0.375	
ρ_{gv}	green leaf reflectance to vis	0.1	
ρ_{bv}	non-green veg. reflectance to vis.	0.22	
ρ_{gn}	green leaf reflectance to nir	0.4	
ρ_{gn}	non-green veg. reflectance to nir	0.48	
V_{max0}	maximum rubisco velocity (μmol$m^{-2}s^{-1}$)	$1x10^{-4}$	$3x10^{-5}$
ϵ	quantum efficiency	0.08	0.05
m	Ball-Berry slope parameter	9	4
b	Ball-Berry leaf-scale intercept	0.01	0.04
A_θ	rate-limiting assimilation colimitation parameter	0.98	0.80
B_θ	rate-limiting assimilation colimitation parameter	0.95	0.95
T_{rda}	leaf respiration parameter	1.3	
T_{rdm}	leaf respiration reference temperature (K)	328.16	
r_{cp}	leaf respiration parameter	0.015	
T_{rop}	assimilation kinetics reference temperature (K)	298.16	
s_{LT}	low temperature stress reponse parameter	0.2	0.3
T_{LT}	low temperature stress threshhold (K)	281.16	288.16
s_{HT}	high temperature stress response parameter	0.3	0.3
T_{HT}	high temperature stress threshhold (K)	308.16	313.16

Table 2.2: Upper boundary conditions and prognostic variables.

	Upper boundary conditions(atmospheric data)
$pCO2_m$	PBL mixed layer CO2 partial pressure (often assumed constant)
V_b	Downwelling direct beam visible radiation
V_d	Downwelling diffuse visible radiation
N_b	Downwelling direct beam near infrared radiation
N_d	Downwelling diffuse near infrared radiation
L_d	Downwelling longwave infrared radiation
P_{ls}	Largescale stratiform precipitation
P_{cu}	Convective precipitation
T_m	PBL mixed layer temperature
q_m	PBL mixed layer water vapor mixing ratio
V_m	PBL mixed layer horizontal windspeed
p_s	Surface pressure
	Prognostic variables
$pCO2_a$	Canopy airspace CO2 partial pressure
T_a	Canopy airspace temperature
e_a	Canopy airspace vapor pressure
T_c	Canopy temperature
T_g	Ground Temperature
$T_d(-5:0)$	Snow layer temperatures
$T_d(1:10)$	Soil layer temperatures
M_{lc}	Liquid water mass on the canopy
M_{ic}	Snow mass on the canopy
M_{lg}	Liquid water mass in the ground puddle storage
$w_i(-5:0)$	Snow layer ice mass
$w_l(-5:0)$	Liquid water mass within the snow layers
$z_d(-5:0)$	Snow layer depths
$w_i(1:10)$	Soil layer ice mass
$w_l(1:10)$	Soil layer liquid water mass
r_s	Canopy scale stomatal resistance

rect beam, visible and near infrared.

Prognostic variables (Table 2.2) are computed within SiB3 by way of two matrices, one which handles prognostic canopy airspace temperature and water vapor, and soil and snow temperatures and another which handles the soil water. There are a few additional prognostic variables, namely snow water, snow mass, and puddle and leaf interception water storage, and soil ice, which are computed outside the matrices. Canopy scale stomatal resistance and canopy airspace carbon dioxide concentration are also computed outside the matrices, within the photosynthesis-conductance submodel. Prognostic variables are propogated from timestep to timestep, being modified by model processes as described above. All other model output, including all surface energy fluxes and carbon fluxes, are computed from the prognostic variables.

2.1.1 The Photosynthesis-Conductance Submodel

The photosynthesis and conductance submodel is explained in Sellers 1996a, and has been compiled from previous work developing the leaf scale model for C3 (Collatz et al 1991) and C4 (Collatz et al 1992) photosynthesis, and scaling the single leaf model to the total canopy (Sellers et al 1992a).

The prognostic canopy-scale stomatal resistance is calculated from the previous timestep's stomatal resisitence adjusted by the steady-state solution to the Ball-Berry conductance-photosynthesis model.

$$r_s(n) = r_s(n-1) + dr_s \tag{2.1}$$

where

$$dr_s = \frac{\Phi}{g_{s,c}} \frac{(1-x)(g_{s,c} - g_{s,\infty})}{(x)g_{s,c} + (1-x)g_{s,\infty}} \tag{2.2}$$

where x is a time damping factor, r_s is canopy scale stomatal resistance to water vapor, $g_{s,c} = \frac{\Phi}{r_s(n-1)}$ is the previous timestep's canopy scale stomatal conductance to CO_2, $\Phi = 44.03\frac{(273.16)p_s}{T_c(1000)}$ is the conversion factor between conductance to CO_2 and water vapor, and $g_{s,\infty}$ is a steady-state solution of the Ball-Berry equation at the canopy scale:

$$g_{s,\infty} = m\frac{h_s A_n}{c_s} + b(F_{s,w} N L_T) \tag{2.3}$$

where h_s is leaf surface relative humidity, c_s is leaf surface carbon dioxide mole fraction, and A_n is the full canopy carbon assimilation rate. The parameters m and b are empirical, and are time invariant parameters (Table 2.1). The C4 m is lower because these plants are able to gather more carbon for a given amount of water loss than are C3 plants (Sellers et al 1992b). The table value of b changes into a canopy scale, soil water dependent minimum stomatal conductance when multiplied by N (greenness fraction of the canopy), L_T (total leaf area index), and $F_{s,w}$ (soil water stress factor).

The leaf to canopy scaling developed by Sellers et al 1992a is based on the assumption that plants distribute photosynthetic resources within the canopy according to the amount of light that on the mean reaches each part of the canopy. Hence, the photosynthetic capacity of the plants will be highest at the top of the canopy, and scale down within the canopy according

to Beer's law. The top-leaf to canopy scaling equation derived from this assumption multiplies the top-leaf assimilation rate by a canopy light use efficiency parameter.

$$A_n(canopy) = A_n(leaf) \cdot \Pi \tag{2.4}$$

$$\Pi = \frac{fPAR}{k_\Pi} \tag{2.5}$$

where fPAR is a satellite derived canopy parameter, the fraction of incident photosynthetically active radiation (PAR) attenuated by the canopy, and k_Π is a daily mean solar-angle dependent canopy extinction coefficient.

The leaf scale model of net assimilation of carbon was originally developed in Farquhar et al 1980 for C3 plants, and presented in Collatz et al 1991. Collatz et al 1992 added a net assimilation model for C4 plants. These models are described in detail below. In the case of a canopy that is mixed C3 and C4, seperate r_s and $A_n(canopy)$ values are calculated (using the appropriate A_n model from below) as if the entire canopy were C3 or C4. The full canopy values of $A_n(canopy)$ and r_s are then simply the weighted average of the C3 and C4 values

$$\mathbf{X} = \mathbf{X}_{\mathrm{C3}}\mathbf{F}_{\mathrm{C3}} + \mathbf{X}_{\mathrm{C4}}\mathbf{F}_{\mathrm{C4}} \tag{2.6}$$

where $\mathbf{X}$ is the variable and $\mathbf{F}$ is the fraction of canopy (Colello et al 1998, Hanan et al 2005).

Photosynthesis is based on three limiting rates, which are somewhat different for C3 and C4 plants. For C3 plants, there is a Rubisco limited rate,

a light limited rate, and a sugar storage and export limited rate.

$$\Omega_c = \frac{p_i - \Gamma_*}{p_i + K_r}(F_{s,w})(F_{s,HT})V_{max0}(2.1)^{Q_T} \quad (2.7)$$

$$\Omega_e = \frac{p_i - \Gamma_*}{p_i + 2\Gamma_*}(PAR)\ \epsilon\ (1 - \delta_{G,V} - \alpha_{G,V}) \quad (2.8)$$

$$\Omega_s = \left(\frac{1}{2}\right)(F_{s,w})(F_{s,LT})V_{max0}(1.8)^{Q_T} \quad (2.9)$$

$F_{s,HT}, F_{s,LT}, F_{s,w}$ are high temperature, low temperature, and soil water stress factors, between zero and one. If the stress factor is one, there is no stress, and photosynthesis is uninhibited by that environmental variable. If the stress factor is zero, the stress has completely shut off photosynthesis. $Q_T = 0.1(T_c - T_{rop})$ is used to calculate the dependence of enzyme activity on temperature (under unstressed conditions), where T_{rop} is a time invariant parameter and T_c is canopy temperature. ϵ is the quantum efficiency for use of absorbed visible light, $(PAR)(1 - \delta_{G,V} - \alpha_{G,V})$, where $\delta_{G,V}$ and $\alpha_{G,V}$ are transmittance and reflectance of PAR by green leaves. p_i is leaf internal CO2 partial pressure. Γ_* is a temperature dependent photorespiration term, which reflects the manner in which oxygenation catalysis by Rubisco more heavily outcompetes the carbon assimilating carboxylation catalysis under high temperature. K_r is a temperature dependent Michelis-Menton Rubisco enzyme kinetics parameter. Finally, V_{max0} is the time invariant maximum Rubisco limited assimilation rate. Maximum Rubisco velocity and quantum efficiency are both higher in C3 plants than in C4 plants, since C3 plants are more efficient assimilators under ideal environmental conditions (Collatz et

al 1998).

For C4 plants, carbon assimilation is sequestered into the high CO2 bundle sheath cells within the leaf, as catalyzed by the enzyme PEP Carboxylase. Photosynthesis is a function of three limiting rates: a Rubisco limited rate, a light limited rate, and a PEP Carboxylase limited rate (which is the only rate dependent on p_i). Photorespiration (Γ_*) has been eliminated.

$$\Omega_c = (F_{s,w})(F_{s,T})(2.1)^{Q_T} V_{max0} \tag{2.10}$$

$$\Omega_e = (PAR)\epsilon(1 - \delta_{G,V} - \alpha_{G,V}) \tag{2.11}$$

$$\Omega_s = F_{s,w} V_{max0} \frac{(1.8)^{Q_T}}{5} p_i \tag{2.12}$$

In this case, low and hight temperature stress factors have been combined into a single total temperature stress term, $F_{s,T} = \frac{1}{((1/F_{s,HT})+(1/F_{s,LT}))}$.

Total gross assimilation is roughly equal to Miminum$(\Omega_c, \Omega_e, \Omega_s)$, but not exactly. The transition between limiting rates is softened by using time invariant colimitation factors (A_θ, B_θ in Table 2.1) in a nested pair of quadratic functions of the three limiting rates. Net leaf assimilation of carbon dioxide is calculated as gross assimilation minus leaf respiration, which is a function of canopy temperature, Rubisco V_{max0}, and soil water stress.

The calculation of soil water stress has been modified from SiB2. Total plant available water of the entire soil column is calculated along with the maximum possible total plant available water. For a single soil layer, the

plant available water is equal to

$$(\theta - \theta_{WP}) \cdot \rho dz$$

where θ is the volumetric water content, θ_{WP} is volumetric water content at permanent wilting point, ρ is the density of water, and dz is the layer thickness. Maximum plant available water is equal to

$$(\theta_{FC} - \theta_{WP}) \cdot \rho dz$$

where θ_{FC} is the volumetric water content at field capacity, above which gravitational drainage becomes too fast for plants to capture that water (Cassel and Nielsen 1986). Wilting point and field capacity are based on soil texture. After summing up all layers, total water stress is calculated as

$$F_{S,W} = \frac{\left(\frac{PAW}{PAW_{max}}\right)(1 + \sigma_w)}{\frac{PAW}{PAW_{max}} + \sigma_w} \tag{2.13}$$

σ_w is a tunable parameter, currently set at 0.2, but capable of ranging from 0.1 to 1. At a σ_w of 0.2, the stress factor stays negligible (near 1) at $\frac{PAW}{PAW_{max}}$ values above 0.5, dropping off sharply below 0.3. At σ_w nearer to 1, the stress curve would be more linear, with more stress at all water contents. Indeed, with σ_w of 0.2, soil water stress very rarely goes below 0.8 at these ARM-CART experiments. This stress model is a modification of that used by Colello et al 1998 and Hanan et al 2005, and was developed by Liu 2004.

2.1.2 Adjusted turbulent flux components

Sensible, latent, and carbon fluxes are calculated using a resistance-potential difference assumption, where

$$F = \frac{\Delta q}{r} \tag{2.14}$$

Potential is q, which is proportional to temperature, vapor pressure, or carbon dioxide partial pressure. Resistance is r (Sellers et al 1996a). Canopy resistance is one of several resistances that are summed in the calculation of total resistance to a given flux. Other resistances include aerodynamic resistances and resistance to water vapor emission by the soil.

Latent and sensible heat fluxes from the canopy airspace to the mixed layer are calculated by SiB3 via a resistance-potential difference equation, as are various fluxes from the surface into the canopy airspace. These include sensible flux from the canopy, snow, and ground (H_c, H_{sn}, H_g), latent flux from wet or snow covered leaves, ground snow, and ground puddles (LE_{ci}, LE_{sn}, LE_{gi}), top layer soil evaporation (LE_{gs}), and transpiration (LE_{ct}).

2.1.3 Hydrology within the Canopy and Snow

SiB3 continues with the SiB2 treatment of convective and largescale precipitation within the canopy. A snow model has been adopted from CLM, including water movement through the snow, melting, freezing, compaction of interior snow layers, and the division of the snow into 1 to 5 individual

layers (Dai et.al.2003). Because snow is only of minor importance in the ARM-CART SGP region, readers are referred to the CLM literature for details about the snow. It shall suffice to say here that precipitation, after having been propogated through the canopy, is delivered either to the liquid puddle storage on the ground, or to the top layer of the snow. In the latter case, water then moves through the snow, possibly undergoing phase change along the way, and finally reaches the ground puddle storage upon exiting the bottom snow layer.

2.1.4 Soil Hydrology and Thermal Models

Soil thermal and hydrological parameters are set according to soil texture, and then modified by the soil water content. The soil water retention curve, relating matric potential to volumetric water content is that described in Clapp and Hornberger 1978

$$\psi = \psi_s(\theta/\theta_s)^{-b} \tag{2.15}$$

Porosity, saturated matric potential, b, and saturated hydraulic conductivity are calculated directly from texture (Cosby et al 1984)

$$\theta_s = 0.489 - 0.00126(\%sand) \tag{2.16}$$

$$\psi_s = -0.01 \cdot 10^{(1.88-0.0131(\%sand))} \tag{2.17}$$

$$b = 2.91 + 0.159(\%clay) \tag{2.18}$$

$$K_s = 7.0556 \cdot 10^{-6.884-0.153(\%sand)} \tag{2.19}$$

Wilting point and field capacity are assigned via the Clapp and Hornberger soil water retention curve, using matric potentials of -1500 and -15 kPa, respectively. A wilting point matric potential of -1500 kPa is widely used, and is quite safe because matric potentials within the range of -800 and -3000 kPa yield roughly the same volumetric water content (Cassel and Nielsen 1986). Field capacity is more difficult to define, and the matric potential selected has a larger impact on the resulting volumetric water content. Fundamentally, any water content in excess of field capacity will not be accessible to plants because it will drain quickly. In investigations of various soil textures, the field capacity should be somewhere between -5 and -50 kPa, with more negative values being appropriate for finer soils (Cassel and Nielsen 1986). Field capacity matric potential is a tunable parameter which may have significant effects on soil water stress, as a more negative field capacity will yield less stress for a given water content.

Soil layers thicken with depth, as in CLM (Table 2.3). Also adapted from CLM, the percentage of roots in each layer is defined by an exponential function

$$f_{root}(j) = \frac{e^{-k_r z(j-1)} - e^{-k_r z(j)}}{1 - e^{-k_r z(nsoil)}} \tag{2.20}$$

where $z(j)$ is the depth of the bottom of the j_{th} layer, $nsoil = 10$ is the bottom soil layer, and k_r is dependent on vegetation type. For grasslands, the choice of k_r yields a distribution more concentrated in higher layers than

would occur in a forest (Table 2.3).

Table 2.3: Soil layer thickness, depth, and root fraction for the ARM-CART SGP simulations

Level	**Thickness(cm)**	**Node Depth(cm)**	**% of total Roots**
1	1.75	0.71	9.3
2	2.76	2.79	13.0
3	4.55	6.23	17.5
4	7.50	11.89	20.8
5	12.36	21.22	20.1
6	20.38	36.61	13.9
7	33.60	61.98	5.7
8	55.39	103.8	1.0
9	91.33	172.8	0.1
10	113.7	286.5	<0.1

The soil thermal equation, as in CLM, is

$$c\frac{\partial T}{\partial t} = -\frac{\partial F}{\partial z} \tag{2.21}$$

with the effects of phase change accounted for after solving the finite difference form matrix equation (Dai et al 2003). Here, T indicates layer temperature, and c is the heat capacity. The downward energy flux in the layer, $F = -\lambda\frac{\partial T}{\partial z}$, where λ is the thermal conductivity of the soil layer. Thermal conductivity and heat capacity are calculated from soil texture and soil water content.

Ground heat flux (G) is diagnosed from the solution to the prognostic soil temperature equation, computed as the sum of the time rate of change in temperature of the top soil layer plus the energy flow out the bottom of

that layer. Neglecting snow, for clarity,

$$G = \frac{c(1)dz(1)dT(1)}{\Delta t} + \lambda(1)(T(1) - T(2)) \tag{2.22}$$

As in CLM, soil water is prognosed in all layers simultaneously in a tridiagonal matrix, which results from approximating numerically the soil water equation,

$$\frac{\partial \theta}{\partial t} = \frac{\partial}{\partial z}\left(K\left[\frac{\partial \psi}{\partial z} - 1\right]\right) - E \tag{2.23}$$

where θ is volumetric liquid water, K is hydraulic conductivity, ψ is matric potential, and E is evaporation out of the layer. Hydraulic conductivity is calculated from its saturated value by the formula described in Campbell 1985.

$$K = K_s\left(\frac{\theta}{\theta_s}\right)^{2b+3} \tag{2.24}$$

Evaporation from most layers is entirely transpiration. Only a certain fraction of total E_{ct} comes out of any particular layer, depending on root density and water availability,

$$E(j) = T_r(j)E_{ct} \tag{2.25}$$

$$T_r(j) = \frac{T(j)}{\sum_{j=1}^{10} T(j)} \tag{2.26}$$

$$T(j) = \frac{\theta_{FC}}{\theta(j)}\left(\frac{\theta(j) - \theta_{WP}}{\theta_{FC} - \theta_{WP}}\right) f_{root}(j) \tag{2.27}$$

However, in the top layer, transpiration and direct evaporation compete,

with their sum not allowed to remove any more than half of the water. Direct evaporation is assumed to take precedence, with transpiration limited to what is left after that. But E_{ct} is still limited by wilting point and root density, as specified in the above formulation of $T(j)$. Therefore, total evaporation out of the top layer is given by

$$E(1) = E_{gs} + T_r(1)E_{ct} \tag{2.28}$$

and forced to never exceed half of the water currently in the layer.

2.1.5 Calculating Vegetation Parameters from NDVI

The fraction of incident PAR absorbed by the canopy (fPAR) is one of several time varying vegetation parameters used by SiB3. Total leaf area index per unit ground area (L_T), fraction of total leaf area that is green(N), and several aerodynamic parameters are also calculated monthly from NDVI, and interpolated to daily values. A time invariant parameter, the fraction of ground covered by green and non-green vegetation (σ_V) is also calculated from NDVI data.

The use of NDVI in SiB3 follows Los et al 2000, which is a slight modification of the method described in Sellers et al 1996b. This section will describe the method of calculating fPAR, L_T, N, and σ_V. Readers are referred to Sellers et al 1996b for a description of aerodynamic parameter calculation.

The initial step takes advantage of a linear relationship between fPAR and

NDVI. Los et al 2000 determined that the the average of a linear fit between fPAR and NDVI $= \frac{\rho_N - \rho_V}{\rho_N + \rho_V}$ and a linear fit between fPAR and SR $= \frac{1+\mathrm{NDVI}}{1-\mathrm{NDVI}} = \frac{\rho_N}{\rho_V}$ is better than either linear fit alone, even though the two indecies are not independent. NDVI and SR (Simple Ratio) are ratios between reflectances in the near infrared and red visible, as expressed above. They are both larger when the vegetation is thick, because vegetation reflects highly in the near infrared while absorbing red visible wavelengths (Holben 1986). The resulting fPAR equation is

$$fPAR = \frac{1}{2}\left(0.02 + 0.94\frac{\mathrm{SR} - \mathrm{SR}_{\mathrm{min}}}{\mathrm{SR}_{\mathrm{max}} - \mathrm{SR}_{\mathrm{min}}} + 0.94\frac{\mathrm{NDVI} - \mathrm{NDVI}_{\mathrm{min}}}{\mathrm{NDVI}_{\mathrm{max}} - \mathrm{NDVImin}}\right) \tag{2.29}$$

The parameters designated by min and max are biome and NDVI dataset dependent parameters, and are meant as bare canopy and fully green canopy vegetation indecies, respectively. These are determined statistically as the 2nd and 98th percentiles, respectively, of NDVI values observed globally throughout each particular biome for the entire NDVI dataset record (Sellers et al 1996). In the above equation, the maximum possible fPAR is assumed to be 0.95, while the bare ground fPAR is assumed to be 0.01.

But this is only the first guess on fPAR, which is later readjusted according to Beer's Law, based on the vegetation parameters L_T, N, and σ_V.

Assuming that upon death or dormancy, vegetative material does not desintegrate, but remains covering the bare soil, σ_V is assumed to be proportional to the maximum first guess fPAR observed over a number of years.

This fPAR is divided by the maximum possible fPAR, 0.95 (Sellers et al 1996b).

The green leaf area index is assumed to vary exponentially with the first guess fPAR

$$L_g = \frac{ln\left(1 - \frac{fPAR}{\sigma_V}\right)}{ln\left(1 - 0.95\right)} L_{Tmax} \tag{2.30}$$

where L_{Tmax} is a biome dependent maximum possible leaf area index (Sellers et al 1996b).

Total leaf area index is calculated as the sum of a stem area index, green leaf area index, and dead leaf area index. Stem area index represents non-photosynthetic structural material, and is assumed to be time invariant, biome dependent, and no bigger than 0.05. Dead leaf area index is derived from green leaf area index, assuming that all dead leaves come from leaves that were formerly green. Dead leaves are assumed to all decay after one month, and only be in existance if the canopy is in a senescing mode; if L_g is increasing, L_d is assumed to be 0.0001, while if L_g is decreasing,

$$L_d = 0.5 \cdot [L_g(n-1) - L_g(n)]$$

This behavior is reasonable for a forest, but in a grassland, there are two potential problems. First, grasses develop a significant amount of time varying, non-photosynthetic flowering and fruiting material. This material never was green leaf, so total leaf area index may be underestimated. Secondly, dead material lasts much longer in a grassland than one month. An alter-

nate treatment of dead leaves was tested at ARM-CART, using a formulation based on that used by CLM (Zeng et al 2002). Here, dead leaves are retained from month to month, decaying at a given rate. But, as in standard SiB3, this is only if the green leaves are decreasing; if L_g is increasing, $L_d = 0.0001$. Otherwise,

$$L_d(n) = \alpha L_d(n-1) + 0.5 \cdot [L_g(n-1) - L_g(n)]$$

The decay parameter α was assumed near 1.0 so that most dead material would be retained until canopy regrowth in the late winter. Total leaf area index and greeness fraction are calculated as in Sellers et al 1996b

$$L_T = \sigma_V (L_g + L_d + L_s) \tag{2.31}$$

$$N = \frac{L_g}{L_T} \sigma_V \tag{2.32}$$

Finally, fPAR is recalculated using Beer's Law with a monthly varying canopy extinction coefficient, the same that is used in the canopy photosynthesis model

$$fPAR = \sigma_V \left(1 - e^{-k_\Pi \frac{L_T}{\sigma_V}}\right) \tag{2.33}$$

where k_Π is dependent on greenness fraction N.

2.2 Input Datasets for the ARM-CART region

2.2.1 The Experimental Design of the Offline Runs

Nine sites were investigated, running SiB3 in uncoupled mode, driven by locally observed meteorology and radiation.

AmeriFlux Tallgrass

The University of Nebraska at Lincoln (UNL) native tallgrass prairie site flux data were available at the Oak Ridge National Laboratory AmeriFlux DAAC

`http://public.ornl.gov/ameriflux/data-access-select.shtml`

This site will now be referred to as the AmeriFlux native prairie site.

As explained in Chapter 1, a modified version of SiB2 has already been compared to flux data at this site for 1997-1998 (Hanan et al 2005). In this thesis, only 1998 is analyzed because of AmeriFlux data availability. The meteorology and radiation data compiled for Hanan et al 2005 , however, were available for 1997-1998, which was taken advantage of in model spinups. These data were half hourly, and had been collected at 4.5 m (on the same height as the flux data), and filled to make a continuous time series.

Three experiments were run: one using the standard Sellers et al 1996b time invariant biophysical parameters for the C4 grassland biome along with

8km GIMMSg NDVI data, one using NDVI but the time invariant parameters of Hanan et al 2005, and one using the Hanan et al 2005 LAI, gLAI, fPAR monthly surface observations and time invariant parameters. All three simulations used a time varying C4 fraction, starting at 0.3 in April, reaching 0.5 in May, and ramping up by 0.1 every month through October, and remaining at 1.0 from October through March. The locally observed soil texture was a silty clay loam, which was assumed to be 10% sand and 39% clay (Sellers et al 1996b).

ARM Sites

Table 2.4: Sites included in this Thesis, their locations, vegetation description, and soil texture (percent sand, percent clay)

Code	**Lat(N)**	**Lon(W)**	**Veg**	**Sand**	**Clay**
OK TG	36.930	96.680	native prairie	10.00	39.00
E04	37.953	98.329	pasture	91.84	4.79
E07	37.383	96.180	pasture	11.72	40.18
E09	37.133	97.266	pasture/wheat	33.76	20.94
E12	36.841	96.427	native prairie	63.56	10.12
E13	36.605	97.485	pasture/wheat	18.81	42.69
E15	36.431	98.284	pasture	92.03	6.15
E22	35.354	98.977	pasture	5.77	45.40
E25	35.245	96.736	pasture	55.99	10.64

Eight ARM sites were chosen on the basis of having reliable flux data during the 1999-2000 testing period (D.R.Cook, pers. comm.), which is when both 1km SPOT NDVI and filled hourly SiB3 driver data were available. For spinup purposes, the years 1996-1998, which had also been provided with

filled driver data, were used with GIMMSg NDVI. The filled site SiB3 driver data are currently described on the ARM internet document McCord et al 2004. All data are directly measured, except for longwave radiation, which is inferred from moisture and temperature data.

Table 2.4 provides location, soil texture, and vegetation type information for all of the ARM sites and the AmeriFlux site. Pasture and native prairie were treated identically in all simulations. All sites are entirely pasture, with the exception of E09 and E13, which were near some wheat fields, and so were assumed to be 50% pasture and 50% C3 wheat. Soil textures in percent sand and percent clay were provided by ARM at two to four levels up to a maximum depth of 60 cm at the ARM sites (W. Hargrove, pers. comm.). A single texture was reached by taking the two nearest layers to the SiB3 layer 5 node depth of 21.22cm and linearly interpolating the sand fraction and clay fraction between those two layers. Several experiments were made at each site.

The Standard run consisted of Sellers et al 1996b grassland biophysical parameters as given in Table 2.1, with the exception that the C3 high temperature stress threshhold value was increased 5 degrees to the standard C4 value of 313.16 K, to account for the fact that C3 plants in the hot prairies of Oklahoma and Kansas have enhanced heat tolerance (J.A. Berry, personal communication). The pasture C4 fraction was assumed to vary annualy in the same way as the AmeriFlux site, while the wheat fraction was assumed to be entirely C3. Therefore, sites E09 and E13 varied in C4 fraction between

0.15 and 0.5, while the rest of the sites ranged annually from 0.3 to 1.0.

Other runs included a run where the Sellers et al 1996b C3 heat stress threhhold of 308.16 was used, and a run where pasture was assumed to be 100% C4 year round. Also, the model was tested using GIMMSg 8km NDVI instead of SPOT 1km NDVI, and using SPOT NDVI with the dead leaves retained for the whole autumn using the Xeng et al 2002 dead leaf decay formulation.

2.2.2 NDVI Data Selection

GIMMSg

The GIMMSg global 8km NDVI dataset was derived from AVHRR visible and near infrared bands (channel 1 and 2), in semi-monthly maximum value composites dating back to July 1981, and has been designed to have comparable values in the later years of its record to the newer MODIS and SPOT platforms (Tucker et al 2005). Explicit treatment of atmospheric effects on the NDVI values was limited to volcanic stratospheric aerosols, in order to minimize artificial manipiulation of the data. However, a statistical Empirical Mode Decomposition method was used to remove trends in the raw data caused by orbital drift induced solar zenith angle changes (Pinzon et al 2002, 2005). Aside from a global product, the GIMMSg 8km resolution data have been collected into continental datasets on an Albers Equal Area projection. The North American continental data were used to compile monthly

timeseries of NDVI at each of the 9 sites, from 1996 through 2000, using the maximum of the two semi-monthly values from the 8km pixel containing the locations of Table 2.4. None of these were close enough to the pixel boundary to cause concern, particularly for the ARM sites, whose flux footprint should not exceed 200-300 meters (100 times the instrument height), and should usually be nearly an order of magnitude smaller than that (Heilman et al 1989). The biome-specific $NDVI_{max}$ applicable to the GIMMSg data have been compiled from the global 8 km dataset using the methods of Los et al 2000 (N. Suits, pers. comm.).

SPOT Vegetation

The SPOT Vegetation monthly dataset has a spatial resolution of 1km (Saint et al 1995). The SPOT data used had already been converted from its native projection to a 1km latitude-longitude grid, and the biome-specific $NDVI_{max}$ had been calculated from the North American dataset using the methods of Los et al 2000 (K.Corbin, pers. comm.). The SPOT pixel containing each site was used to compile the site NDVI timeseries, with the flux footprint assumed to be contained within the 1 km grid cell.

2.2.3 Initial Condition Spinup

Initial soil water conditions can significantly affect land surface simulations (Sud et al 2001, Betts et al 1996). Ideally, soil water and all other prognostic variables will be initialized to observed data. But this is rarely

possible for all 10 soil layers. Alternatively, a spinup of the model from an arbitrary starting point (usually saturated soils) is used until an equilibrium condition has been reached (Dai et al 2003). It has also been frequently observed that in the ARM-CART SGP region, simulated soil water takes on the order of months to spinup, not years (e.g. Ghan et al 1997, Sud et al 2001). This result has been confirmed in this study. Repeating a year's run of SiB3 changed the December 31 soil water conditions by at most 1% at the deepest layer.

At all the sites, a saturated soil initial condition was generated by running a single year forcing soils to always be saturated. To complete a spinup at the ARM sites, 1996-1998 was run from saturation using GIMMSg satellite data, and the test period 1999-2000 was run from the end of the spinup. Each individual year was simulated twice, using the first run's "Carbon Respfactor" to distribute respiration within the soil, which forces the year's respiration to very nearly balance the year's net photosythetic uptake (Denning et al 1996a). Only the respiration fluxes (and hence Net Ecosystem Exchange carbon flux) are significantly modified by this practice. At the AmeriFlux site, 1997-1998 was cycled twice, using a saturated initial condition for the first cycle. The first cycle followed by the second 1997 simulation served as a spinup for the second 1998 run, which was what was compared to data. As with the ARM sites, annual carbon balance was enforced.

2.3 Flux and Soil Data in the ARM-CART region

Hourly eddy correlation (EC) latent, sensible, and net carbon fluxes along with net radiation and ground heat flux data were downloaded for 1998 from the AmeriFlux website

`http://public.ornl.gov/ameriflux/data-access-select.shtml`

For the eight ARM sites, half hourly Energy Balance Bowen Ratio (EBBR) latent, sensible, ground heat, and net radiation data were downloaded for 1999-2000 from the ARM archives

`http://www.archive.arm.gov/cgi-bin/arm-archive`

and an hourly quality checked soil temperature and liquid water dataset was downloaded from a special section of the ARM site (McCord et al 2004)

`http://www.archive.arm.gov/Carbon/`

2.3.1 AmeriFlux EC Data

The data were used as is. Previous work using this dataset has indicated that these eddy correlation data have been corrected for sensor seperation, LE density fluctuation, LE oxygen contaimination, H humidity and wind adjustments (Burba and Verma 2001), and for CO2 flux water vapor air density fluctuations (Suyker and Verma 2001). The station used a Radiation and Energy Balance Systems (REBS) Q7 whole spectrum net radiometer. A 5cm deep soil heat flux plate and 0-5cm temperature sensor were used to

derive ground heat flux. Details are provided in Suyker and Verma 2001. In short, the covariances of rapid time fluctuations of vertical wind along with either CO2 concentration, water vapor mixing ratio, or temperature serve as measures of the vertical fluxes of CO2, latent heat, and sensible heat, respectively.

2.3.2 ARM EBBR Data

The ARM Energy Balance Bowen Ratio system (EBBR) uses similar net radiation and ground heat flux instruments to the AmeriFlux site: a whole spectrum net radiometer, and an array of 5 ground heat flux systems whose output are averaged. Bowen Ratio is then estimated by the water vapor and temperature differences between two vertically seperated arms, which are switched in position every 15 minutes to remove sensor bias. The switching mechanism takes 2 minutes, and 13 minutes worth of 30 second observations are used to create the two 15 minute mean Bowen Ratios that are averaged for the unbiased 30 minute mean (Cook 2005, Brotzge and Crawford 2003).

As explained in Fritchen and Simpson 1989, the theory of Bowen Ratio energy balance assumes $R_n = G + H + LE$. Only R_n, G, and the Bowen Ratio $BR = \frac{H}{LE}$ are directly observed. Sensible and latent flux are computed as

$$LE = \frac{R_n - G}{1 + BR} \tag{2.34}$$

$$H = BR \cdot LE \tag{2.35}$$

Assuming that the there are no horizontal energy fluxes, that fluxes have a homogeneous source region, and that the conditions of the local atmosphere are not rapidly changing, the Bowen Ratio is derived from the vertical gradients of temperature and vapor pressure across a small distance (usually about 1 m)

$$BR = \frac{\Delta T}{\Delta e}\frac{K_h}{K_w}\frac{pM_d c_p}{L_{l,v}\left(\frac{e}{p}M_w + \frac{p-e}{p}M_d\right)} \tag{2.36}$$

where K_h and K_w are the heat and water eddy diffusivities, c_p is the heat capacity of dry air, p is pressure, M_d and M_w are the molecular weights of dry air and water vapor. $\frac{pM_d}{\left(\frac{e}{p}M_w+\frac{p-e}{p}M_d\right)}$ is for converting vapor pressure gradient into vapor mass gradient. A commonly used assumption is that $K_h = K_w$, so that the Bowen Ratio measurement system need only supply current measurements of pressure, vapor pressure, and temperature in order to use the formula, the rest of the required quantities being constants. The vertical difference in e will be sufficiently small compared to p that it does not matter which arm's e is used in the vapor pressure to mass conversion factor.

The theory of ground heat flux measurement is analogous to that of SiB3, with ground heat flux assumed to be the time rate of change in top soil layer energy storage plus the flux out the bottom of this layer (5 cm depth in this dataset) :

$$G = C\frac{\partial T}{\partial t}z_2 - \lambda \left.\frac{\partial T}{\partial z}\right|_{z_2} \tag{2.37}$$

where z_2 is 0.05m, C is the 0 to 5 cm soil heat capacity (calculated from soil

texture and water content), and λ is the thermal conductivity of the soil at 5 cm (Brotzge and Crawford 2003). The use of the soil heat flux plate at 5cm implicity requires an assumption that the thermal conductivity of the plate is equal to that of the soil, which adds an uncertainty of about 5% to the flux measurement (Twine et al 2000). Although some sensors attempt to correct for this difference, the ARM sensors do not (Brotzge and Crawford 2003).

The 30 minute mean data were downloaded from the ARM archive, and then all measured quantities including net radiation, soil temperature, soil water, air temperatures and water vapor pressures, and a voltage reading of the automatic sensor exchange mechanism were checked each timestep to see if they fell within the accepted range, published in Cook 2005. If any quantity was incorrect, all R_n, G, BR, H, and LE data were thrown out. Furthermore, if the Bowen Ratio fell within the range -0.45 and -1.6, H and LE data were thrown out because such a Bowen Ratio is sufficiently close to -1.0 that the derived fluxes areunreliable and erratic (because $1 + BR$ in the denominator of the LE forumula is close to 0, yielding fluxes that are extremely and unrealistically sensitive to very small changes in BR) (Cook 2005, Brotzge and Crawford 2003).

2.3.3 Flux System Uncertainties

Numerous studies of EC and EBBR accuracy have been made within the ARM-CART region, some using the FIFE dataset and others using the current ARM network. It should be noted that while the ARM-CART network

uses EBBR systems, the FIFE dataset used systems of a slightly different design, and known by a different name. In general, the EBBR system is one kind of Bowen Ration (BR) system, also known as a Bowen Ration Energy Balance (BREB) system. This is mostly a semantics issue, but each of these acronyms is encountered in the literature.

Despite being probably the best constrained of the variables, net radiation actually has an uncertainty of at least on the order of 10-20 W/m^2 (Brotzge and Crawford 2003, Field et al 1992, Nie et al 1992). This uncertainty would be considerably less were four component net radiation systems (upward and downward longwave and shortwave sensors) used, as the plastic dome architecture of the whole spectrum systems absorbs an uncertain amount of radiation (Field et al 1992). Although newer sensors such as those used in these datasets have improved the dome design to reduce absorption, they are still susceptible to degradation over time (Brotzge and Crawford 2003).

Ground heat flux is more uncertain, which yields an uncertainty in $R_n - G$ of at least 50 W/m^2 (Twine et al 2000), frequently larger (Brotzge and Crawford 2003, Fritschen and Qian 1992). G uncertainty is due to the combination of uncertainties in thermal conductivity, solid matter heat capacity, soil moisture content, and perhaps most importantly a high horizontal soil variability, in such things as pores and roots as well as texture (Brotzge and Crawford 2003, Twine et al 2000, Schneider et al 2003). Differences in $R_n - G = H + LE$ were a significant portion of the discrepancy between side-by-side H and LE results in some FIFE experiments using BR systems (Nie et al 1992, Fristchen

et al 1992).

BR system uncertainties in daily mean latent heat flux and Bowen Ratio were documented at 20% and 30%, respectively (Nie et al 1992). One likely cause of EBBR system uncertainty is the assumption that $K_h = K_w$ (Brotzge and Crawford 2003). Another is the fact that energy balance is forced even though $R_n - G$ may not be correct. Inhomogeneities within the flux sources in an EBBR footprint are another source of uncertainty, given that the EBBR method assumes homogeneity (Fritschen and Simpson 1989).

EC and BR systems have different sources of uncertainty in H, LE and Bowen Ratio. In one ARM-CART SGP study $H + LE$ and $BR = \frac{H}{LE}$ were typically higher in the EBBR system (Brotzge and Crawford 2003). Although the EBBR systems were not exactly right, it was seen that the EC system was underestimating the total turbulent flux, particularly latent heat flux. Because the EC R_n, G, H, and LE data are independently measured, errors in the components can cause an apparent surface energy imbalance. Twine et al 2000 found that $\frac{H+LE}{R_n-G}$ was typically in the 0.7-0.9 range, which corresponds to an energy imbalance of about 100-150 W/m^2. They also showed that carbon uptake was also underestimated by the EC systems (Twine et al 2000). Another source of a difference between EC and EBBR fluxes is the larger and more wind-sensitive flux footprint of the EC system (Fritschen et al 1992, Brotzge and Crawford 2003).

2.3.4 Soil Water and Temperature data

Soil water and temperature at eight levels between 5 and 175 cm were provided by hourly observations from the ARM Soil Water and Temperature System (SWATS), although a few of the sites did not have data from the lowest few layers. As with the AmeriFlux data, these were taken as is, because quality control measures had already been performed(McCord et al 2004).

SWATS design and initial ARM field results are described in Schneider et al 2003, with additional detail and lab calibration results in Reece 1996. All SWATS data are derived from thermocouple temperature measurements taken from within a porous ceramic solid cylinder inserted into the soil. The ceramic acts as a surrogate for the soil, and is assumed to equilibriate to the same temperature and liquid water matric potential as the surrounding soil. Along with an hourly temperature reading, a heat pulse is sent into the ceramic causing a temporary change in temperature, which is a function of the matric potential of the liquid water within the ceramic. Although each sensor has a somewhat different conversion between temperature change and liquid water matric potential, the difference can be eliminated by determining in the laboratory a relationship between the sensor temperature response and a reference temperature response . The formula for matric potential is

$$\psi_m = -0.717e^{(1.788)\Delta T_{ref}} \tag{2.38}$$

where

$$\Delta T_{ref} = m\Delta T_{obs} + b \tag{2.39}$$

Volumetric water content is calculated from matric potential by way of the van Genuchten 1980 soil retention curve

$$\theta = \theta_{ref} + \left[\frac{\theta_s - \theta_{ref}}{\left\{1 + \left[\alpha\left(\frac{-\psi}{100}\right)\right]^n\right\}}\right]^{1-(1/n)} \tag{2.40}$$

where the texture dependent van Genuchten parameters are derived in the laboratory using soil samples taken from the site.

Comparing model output to SWATS soil water data has several complications. First of all, the model only has one soil texture, whereas the data use up to 4 textures varying with depth. Second of all, the different soil retention forumulations between SiB3 and SWATS yields artificial differences between volumetric water contents.

Thirdly, there are particular instances where the SWATS uncertainty is quite high. In soils having a high sand content, the hydraulic conductivity of the ceramic is significantly lower than that in the soil, so the SWATS water will be much more constant in time than is the actual soil water (Schneider et al 2003). This error was largest at the very sandy sites E15 and E04, with absolutely zero seasonal cycle in water at some layers; some error also should be expected at the relatively sandy E25 and E12. Also, the SWATS data overestimates low water contents, particularly drier than -1200 kPa (Reece 1996). Soils this dry were encountered frequently in these experiments in the

summer.

2.4 Using SiB3-SCM at the ARM-CART site

2.4.1 Model Description

A suitable reference to introduce the Colorado State University GCM, with references to parameterization details, is Randall et al 1996. In brief, there are prognostic vertical profiles of potential temperature, water vapor mixing ratio, and zonal and meridional winds. Also surface pressure, boundary layer thickness and TKE, ground temperature, and snow/ice temperature are prognostic. Model paremterizations include convection, a planetary boundary layer, radiative transfer, and large scale cloudiness.

A paper describing the CSU-GCM in single column mode has already been discussed in Section 1.2.3 (Randall and Cripe 1999). To repeat, in single column mode, the model must have lateral boundary conditions of temperature and water vapor prescribed from data, as well as top of the atmosphere radiation. The SCM profiles and surface prognostic variables must be initialized from data or from some sort of spinup.

When SiB3 is run within the SCM, its time invariant and time varying surface parameters are specified just as in the uncoupled SiB3 runs. SCM PBL meteorological variables, precipitation rates, and downwelling radiation (with shortwave already separated into four components) serve as the SiB3 upper boundary conditions. When SiB3 provides the SCM with upwelling

latent and sensible heat fluxes, ground temperatures and surface albedo, the systems are fully coupled. Alternatively, domain representative ARM-CART sensible and latent fluxes and ground temperatures can be given to the SCM, but with SiB3 still being driven by the SCM output and still suplying the SCM with surface albedoes. This run will be referred to as the Prescribed run, whereas the fully coupled run will be designated Coupled. As discussed before, SCM lateral boundary conditions are specified by Revealed Forcing, direct incorporation of observed lateral advective tendencies of temperature and water vapor (Randall et al 1999).

2.4.2 Experiment

Coupled and Prescribed runs were tested using initial atmospheric profiles and lateral forcings appropriate for the year 2000. Prescribed run surface fluxes and ground temperature were taken from ARM observations (M. Branson, pers. comm.). In addition, Mark Branson provided for comparison a Revealed Forcing SiB2-SCM simulation of the year 2000.

The simulation soil type was figured from IGBP sand and clay fractions aggregated up to 1 by 1 degree. A domain average sand and clay fraction was figured by averaging 1 by 1 degree values from 34-38 ° N and from 95-100 ° W. These numbers were then compared to the USDA soil triangle to determine what texture this was (loam), and the USDA triangle mean sand and clay fraction for loam (42% sand, 18% clay) was used as the SiB3 soil texture. Loam turns out to be the texture class deemed most appropriate

to the ARM-CART domain in Sud et al 2001. As evident from the 8 ARM sites in Table 2.4, the ARM-CART site is actually composed of many very different soil textures, so in fact no single number is going to accurately describe the domain. The loam should be as reasonable as any other single soil texture.

The NDVI was calculated monthly for 1996-2000 from the North American continental 8km by 8km GIMMSg dataset. Although the Albers equal area grid is not equivalent to latitude and longitude, the 55 roughly N-S by 50 roughly E-W pixels used to create a single monthly domain-average number ranged from roughly 34° 45' to 38° 30' N and 95° 0' to 99° 45' W, which is slighly bigger than the official ARM-CART domain. The fractional vegetation cover derived from this NDVI timeseries was 0.63, which agrees with the 0.60 fractional vegetation cover deemed most apporpriate for the ARM-CART site by Sud et al 2001. Based on the land use maps provided by ARM on

`http://www.xdc.arm.gov/data_viewers/sgp_surfchar/`

the domain was assumed to be half pasture (with the Hanan et al 2005 time varying C4 fraction) and half winter wheat (all C3).

For a third experiment, SiB3 was run offline from the SCM using the same soil type and NDVI data as in the SCM runs. SiB3 upper boundary conditions were taken from ARM-CART SGP site E13, the ARM-CART SGP central facility. Because of a strong east to west precipitation and moisture gradient in the Southern Great Plains, the E13 meteorology was

assumed to be a fair representative of the region. However, the high spatial variability of convective precipitation means that the E13 precipitation is significantly different from an ARM-CART domain average. Nonetheless, since using a domain averaged precipitation would not be a perfect ARM-CART domain simulation either, this method was deemed appropriate. An experiment at ARM-CART using a different land surface model determined that running the model using domain averaged precipitation data produces significantly different fluxes from a domain average of a grid of 6.25x6.25 km simulations. This occurs because a domain averaged precipitation dataset dilutes all convective rain events (Ghan et al 1997).

The same SiB3 surface initial conditions were used in all three experiments. To generate these conditions, offline SiB3 was run 1996-1999, using a loam and domain average GIMMSg NDVI data as above, and forced by ARM E13 meteorology, starting from saturated soils.

Chapter 3

Results

3.1 The AmeriFlux Tallgrass Site

Table 3.1: The AmeriFlux experiments

Name	**Time Invariant Parameters**	**Time Varying Parameters**
Standard	Sellers et al 1996	GIMMSg 8km NDVI
Calibrated	Site specific (Hanan et al 2005)	GIMMSg 8km NDVI
Local	Site specific (Hanan et al 2005)	Surface Measured

The three AmeriFlux runs had very similar monthly mean latent and sensible heat fluxes and net radiation in 1998 (Fig. 3.1). Overestimation of net radiation in the summer yields latent and sensible heat fluxes that are both overestimated. Latent heat flux is only slightly high, and EC data is likely too low, so the results are reasonable. Sensible heat, however, is overestimated by a less reasonable amount. These energy flux results are similar to those of Hanan et al 2005, except that latent heat flux is no longer

underestimated in July, a result of higher water availablity in SiB3 than in SiB2.

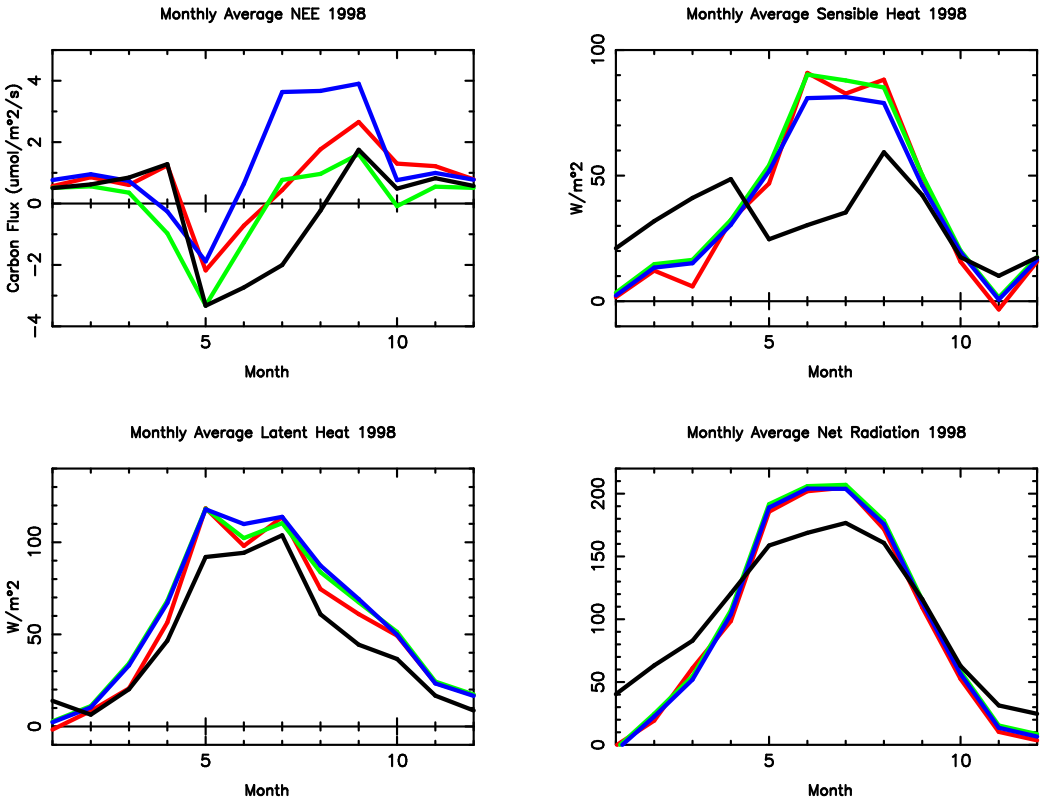

Figure 3.1: 1998 Monthly Mean simulated versus measured results. Data is in black, Standard run blue, Calibrated run green, Local run red.

On the other hand, net carbon dioxide flux into the atmosphere (NEE), was quite different between the experiments (Fig. 3.1). Only the Local run was able to capture the effects of a land management burn in the end of March, because the 8km NDVI data included green vegetation outside the burned area. This can be seen quite clearly in a selection of days from April (Fig 3.2), where the NDVI based runs have much more daytime carbon

uptake than the data or Local run. Meanwhile, latent flux is too high in all three runs, although somewhat improved in the Local run. Soil evaporation was likely overestimated in the Local run.

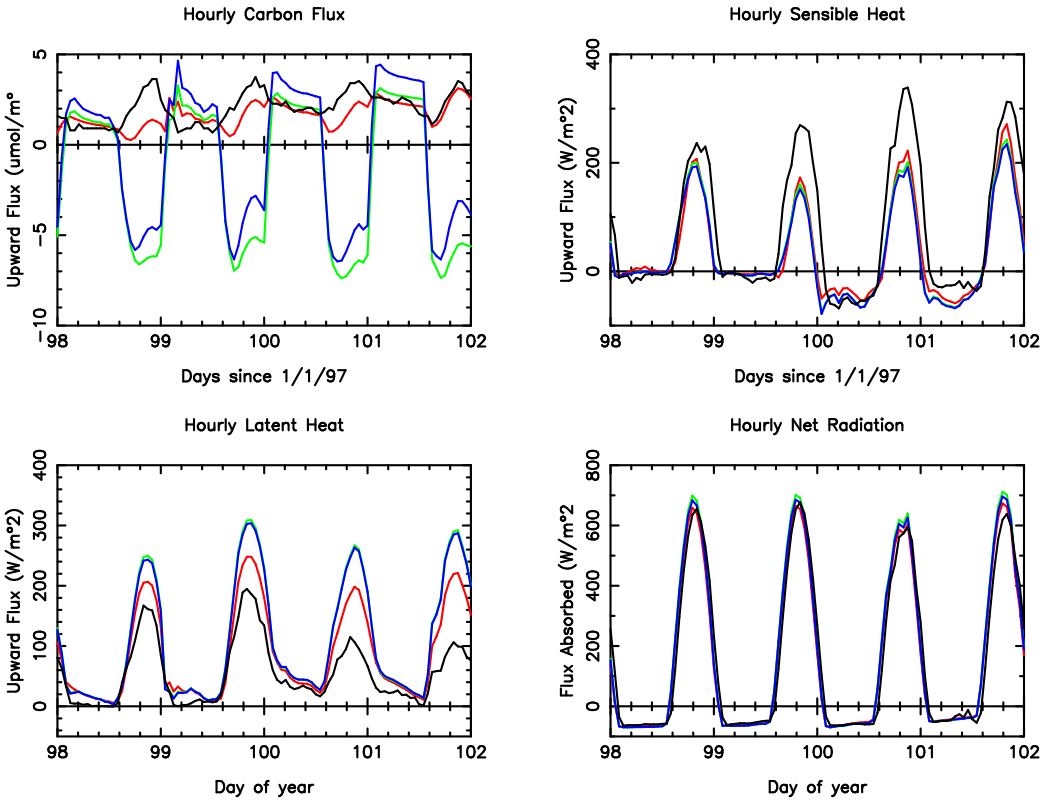

Figure 3.2: Early April hourly NEE, latent heat, sensible heat, and net radiation flux. Data is in black, Standard run blue, Calibrated run green, Local run red.

During the summer, sensible heat flux and NEE indicate that all of the experimental SiB3 runs had too much vegetation stress. As seen from a few days in July, the uptake is severely reduced in the middle of the afternoon (Fig 3.3), along with too much sensible heat. Curiously, although using the

site specific biophysical parameters improves afternoon carbon uptake by 5 or more μmol m^{-2} s^{-1}, there was no corresponding change in the sensible and latent heat fluxes.

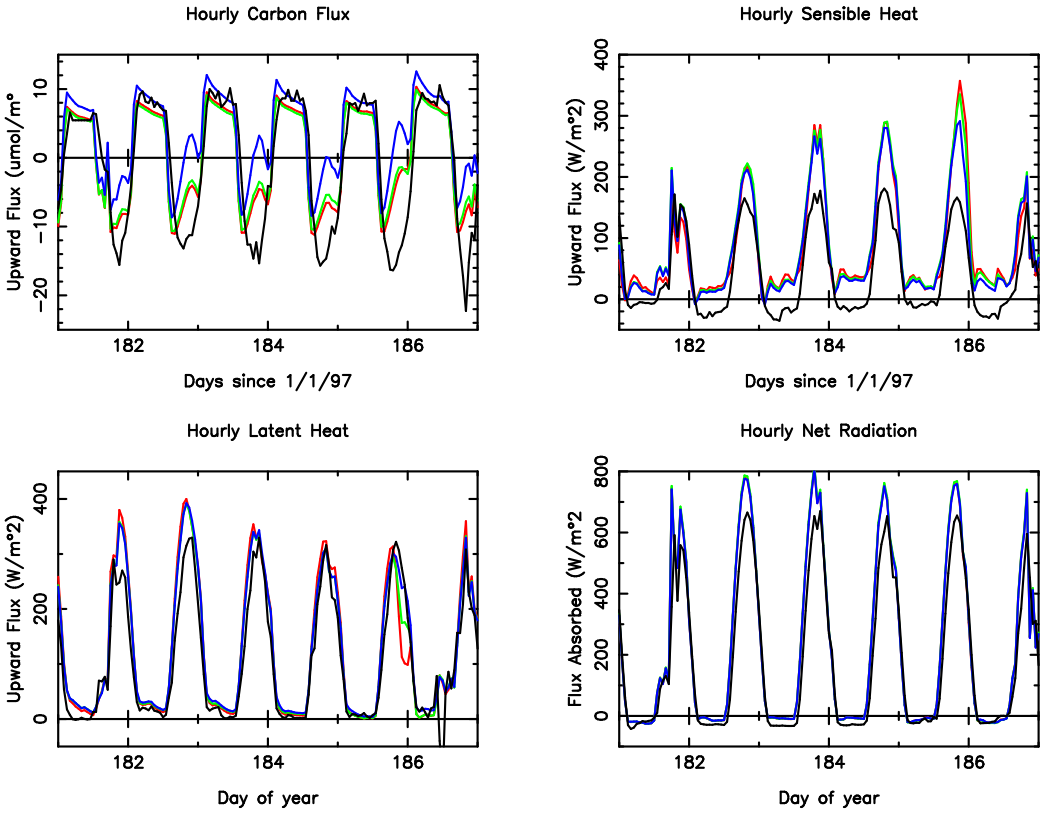

Figure 3.3: Early July hourly NEE, latent heat, sensible heat, and net radiation flux. Data is in black, Standard run blue, Calibrated run green, Local run red.

The parameter $\Pi = fPAR/k$ is representative of canopy greenness and multiplies leaf photosynthesis to scale it to the full canopy (Equation 2.4), while Leaf Area Index (L_T) includes photosynthetic and non-photosynthetic material. The 1997-1998 seasonal cycles of $fPAR/k$, L_T are compared be-

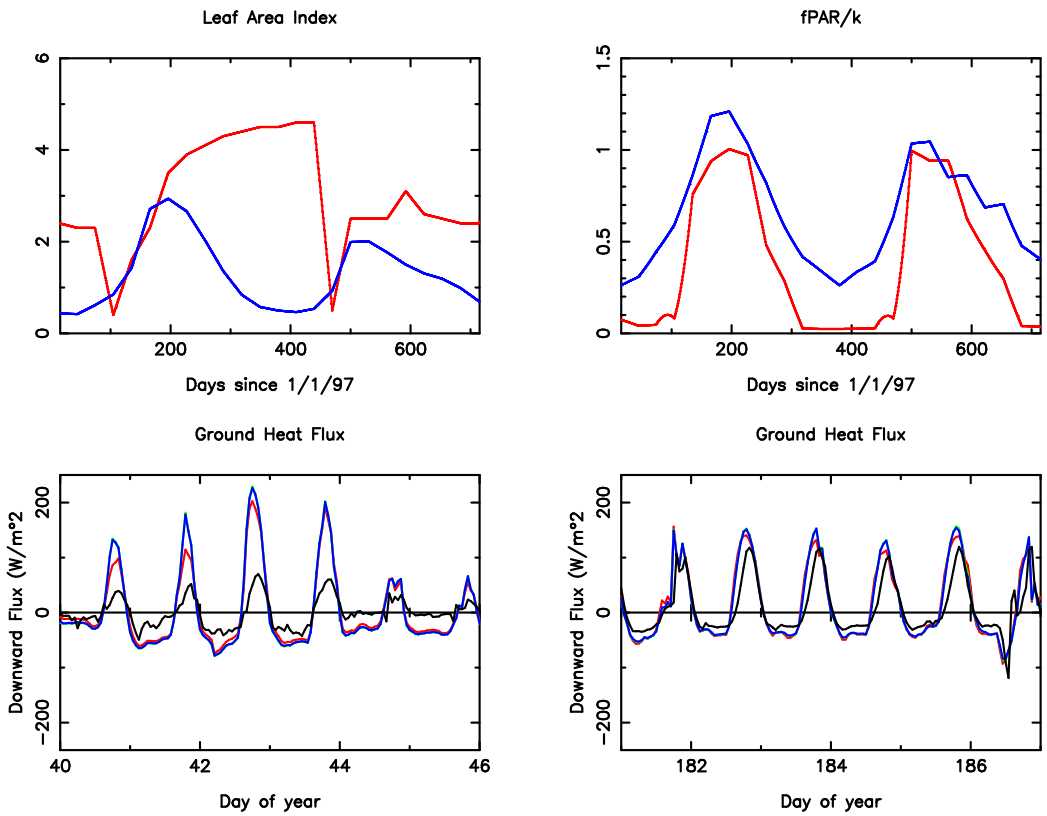

Figure 3.4: NDVI based 1997-1998 vegetation parameters fPAR/k and L_T are in blue (from the Standard Run), while the surface observations of Hanan et al 2005 are in red (Local Run). In the bottom two panels, ground heat flux are compared to the data from two runs in February 1998 (left) and July 1998 (right)

tween the NDVI and Local runs (Fig 3.4). The NDVI $fPAR/k$ does not get low enough in the winter, and is slightly high in the summer. Meanwhile, in the surface data, L_T stays high until the spring burn off, although most of the leaf area is non-photosynthetic during the winter. The NDVI-based L_T inaccurately decreases in the fall because dead leaves are assumed to disappear within a month. The use of local L_T data, with wintertime dead leaves should improve the simulation by increasing shading, and hence decreasing ground heat flux. Indeed, daytime ground heat flux was lowered in February using local L_T, but not by enough (Fig 3.4). As in Hanan et al 2005, the ground heat flux simulation is much better in the summer, when leaf area is mostly green.

A fundamental conclusion is that although site specific biophysical and time varying vegetation parameters substantially improved carbon fluxes, they had less of an impact on energy fluxes at this location.

3.2 The Eight ARM Flux Sites

3.2.1 Standard SiB3 Evaluation

Recall that the Standard SiB3 run for the ARM sites assumed 100% pasture at all sites but E09 and E13, which were half pasture and half wheat. Sellers et al 1996b time invariant biophysical parameters were used, except that C3 vegetation high temperature stress was reduced. Half hourly R_n, G, H,and LE model output were compared to the EBBR data.

Net Radiation

Model net radiation was computed as the sum of the net radiation received by the canopy and the net radiation received by the ground and snow. Comparing the half hourly output to data (Fig. 3.5), there is a good one to one correspondence, but a large scatter of about 350 W/m^2 and a slight positive bias. This tendency to overestimate net radiation is expected from Colello et al 1998 and from the AmeriFlux results. The smooth and relatively well simulated seasonal cycle of 11-15 Central Standard Time (CST) net radiation is similar from site to site (Fig 3.6). Numerous rejected data points, including nearly all sunny daytime data, affected the appearance of the 2000 seasonal cycle at E25.

Latent Heat Flux

Half hourly latent heat flux simulation versus observation has a slope of less than one, with overestimation of night values and underestimation of the highest values (Fig. 3.7).

The seasonality of model error in afternoon mean daily latent heat flux varied considerably from site to site, from overestimated late summer latent flux (E04,E25), to an early onset of autumnal dormancy (E09,E13,E15), to underestimation of latent flux for the whole growing season (E13,E15), to an early seasonal cycle year-round (E12) (Fig. 3.8). This high variability indicates that the sites have key differences between them that are not correctly

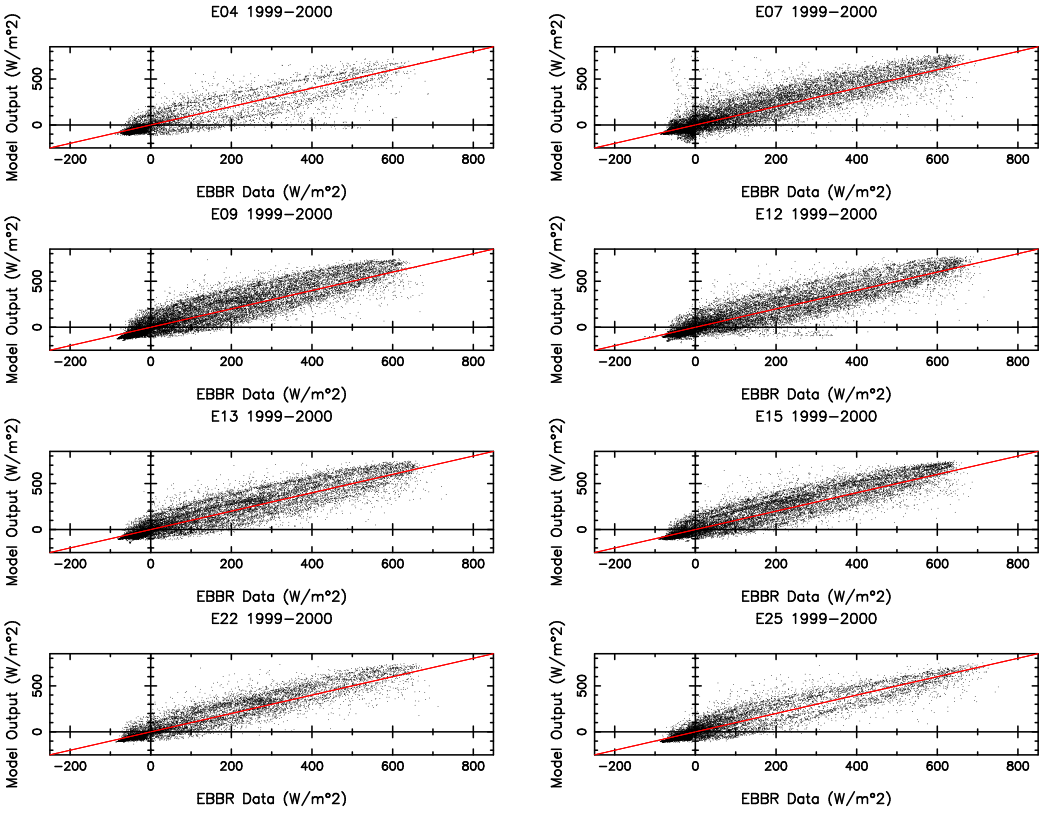

Figure 3.5: Half hourly SiB3 net radiation versus measured net radiation.

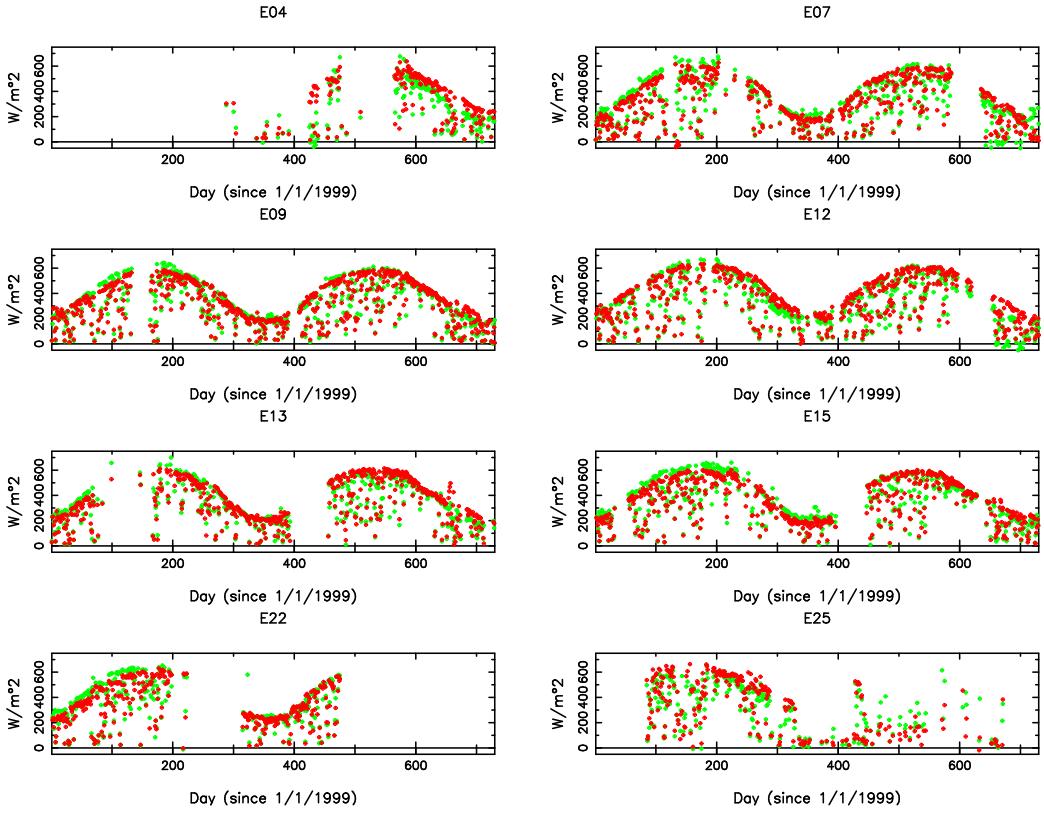

Figure 3.6: Daily mean 11-15 CST net radiation fluxes for 1999-2000, with the EBBR data in red and the model output in green.

captured by the model. Potential sources of the errors in latent flux include incorrect time invariant vegetation parameters, incorrect NDVI-based parameters, and excessive late summer heat stress. Wheras at the AmeriFlux site, latent heat flux was relatively insensitive to the vegetation parameters, this is not necessarily true at all of the sites.

The model does not have enough nighttime dewfall (Fig. 3.9). This was also observed by Hanan et al 2005, and they suggested that a lack of dew is accompanied by an underestimation of early morning latent heat flux, which was observed in the winter here (Fig. 3.10). In the summer, any lack of dew evaporation is masked by high transpiration rates (Fig. 3.11).

While the June 1999 mean diurnal cycles of Fig. 3.11 are very well simulated at most of the sites, most of the August 2000 diurnal cycles have too much vegetation stress in the middle of the day in the model (Fig. 3.12), which explains why daily mean latent flux decreases too early in the year at several sites. Too much C3 vegetation, particularly at E09 and E13 which are assumed half C3 wheat, could explain some of the excessive stress in the late summer. Indeed, it is probably an error to keep these sites at half wheat after wheat harvest: wheat is reduced to zero at this time. Meanwhile, at E04, where late summer latent flux is overestimated, stress in the middle of the day mitigates the situation, suggesting a problem with the time invariant or NDVI based parameters, and perhaps too high a C4 fraction.

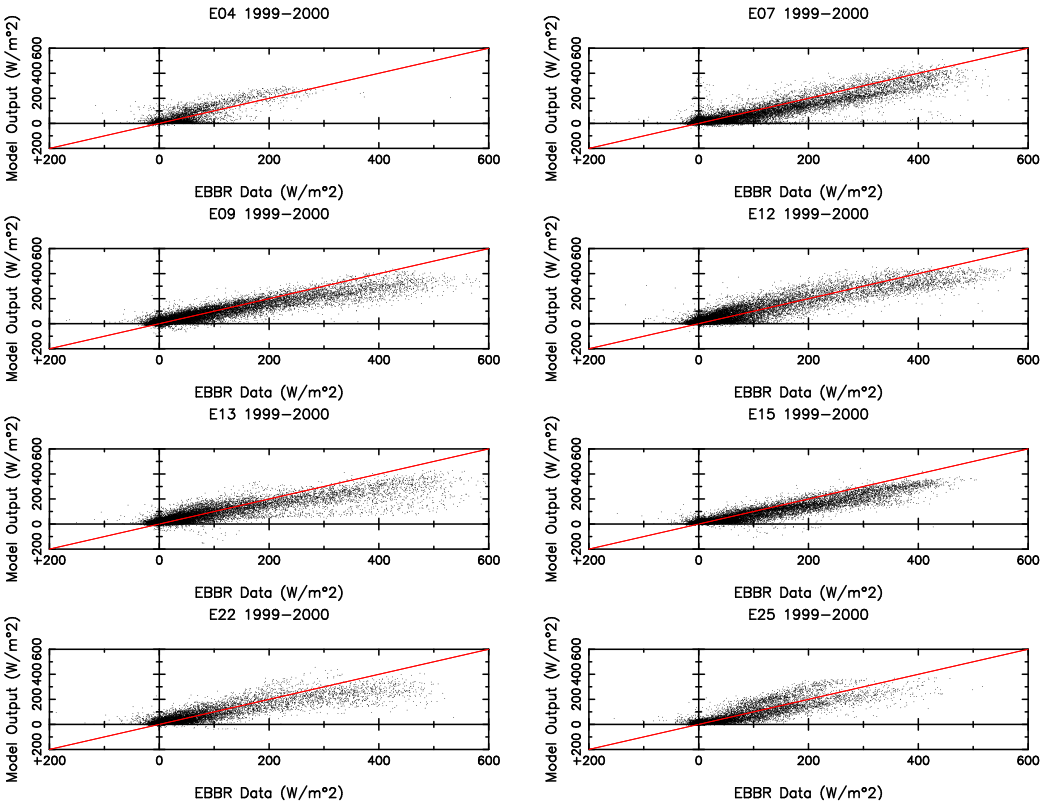

Figure 3.7: Half hourly SiB3 latent heat flux versus observations

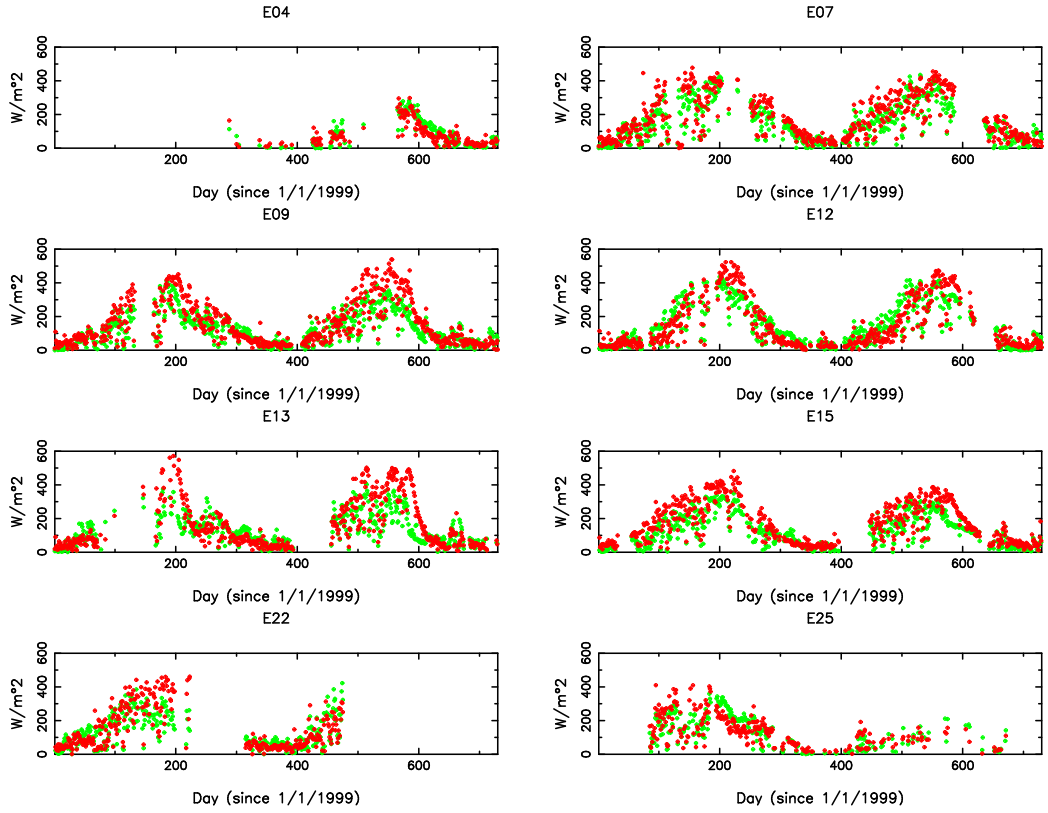

Figure 3.8: Daily mean 11-15 CST latent heat fluxes for 1999-2000, with the EBBR data in red and the model output in green.

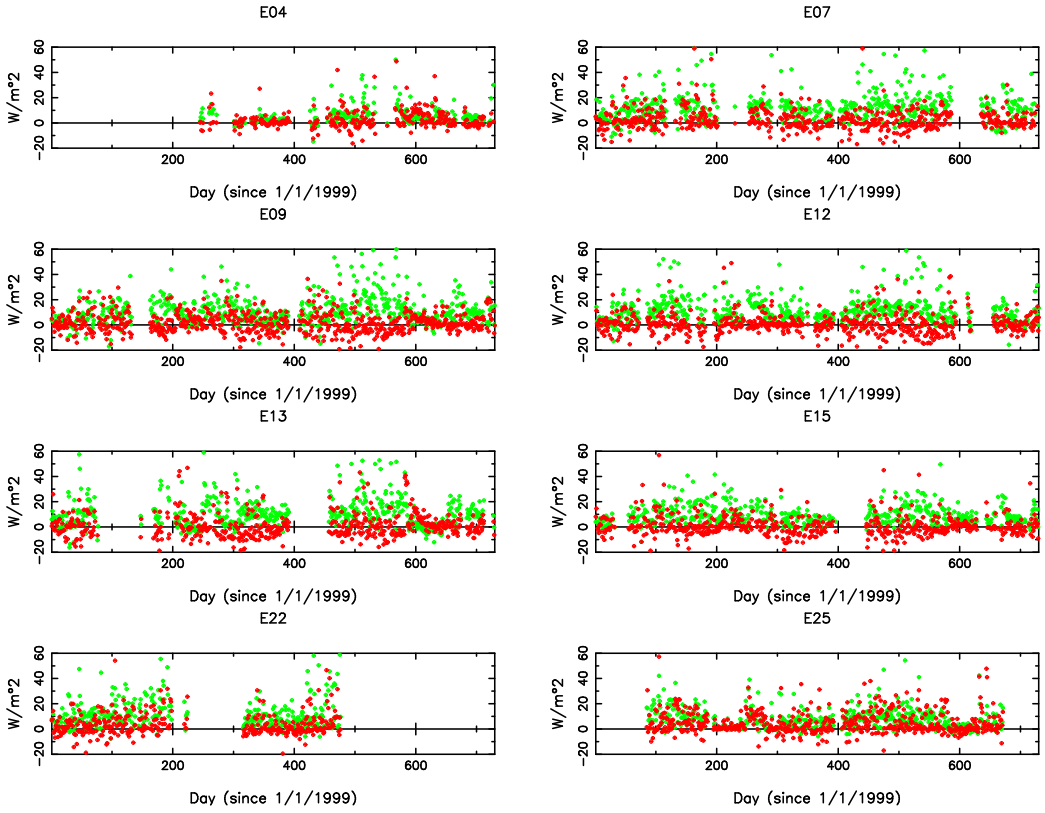

Figure 3.9: Daily mean 23-03 CST latent heat fluxes for 1999-2000, with the EBBR data in red and the model output in green.

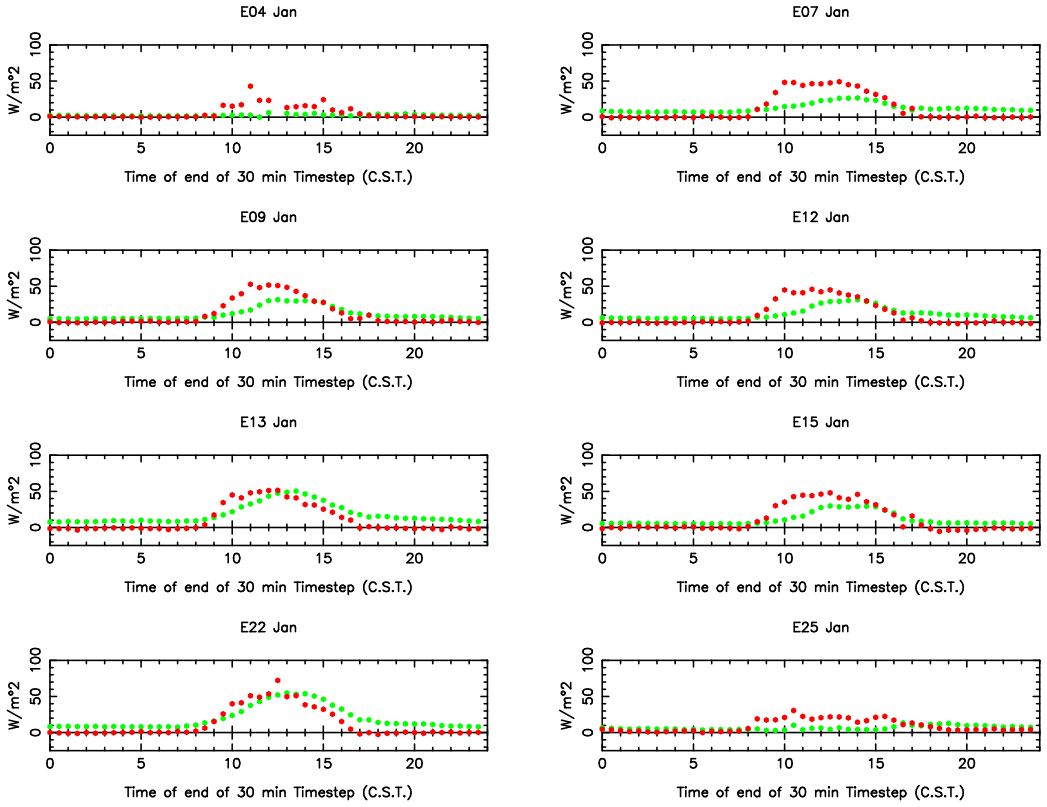

Figure 3.10: Mean latent flux 12AM-12AM CST diurnal cycle for January 2000, data red, model green.

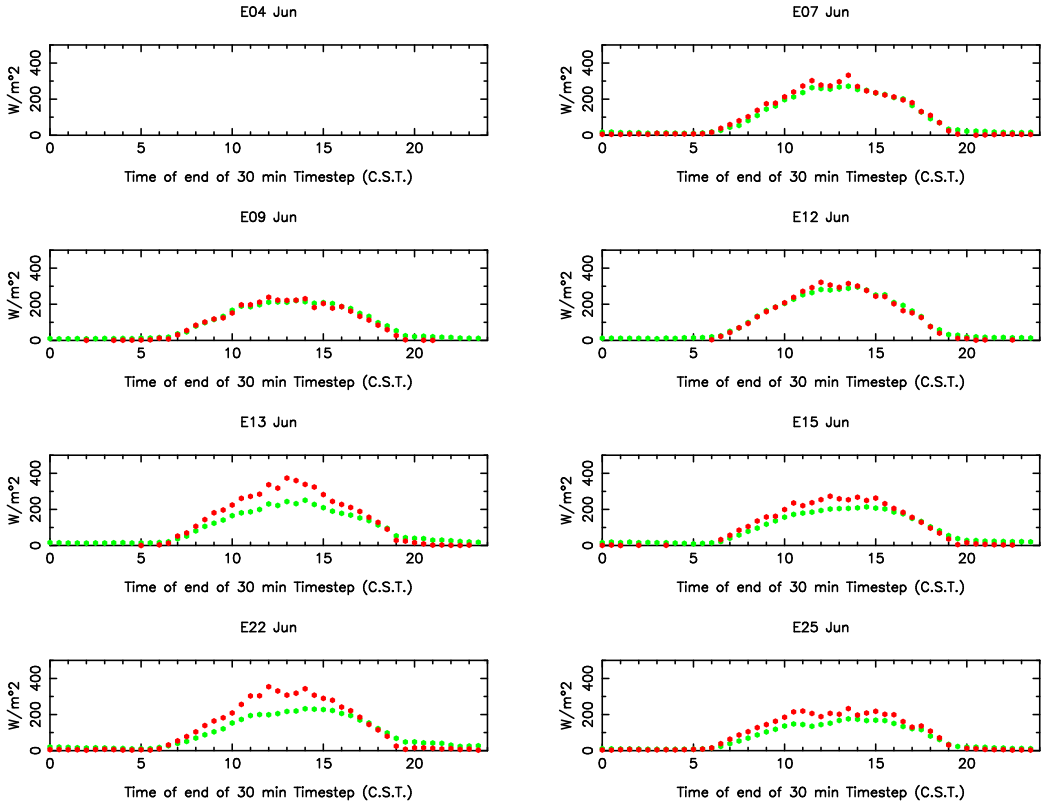

Figure 3.11: Mean latent flux 12AM-12AM CST diurnal cycle for June 1999, data red, model green.

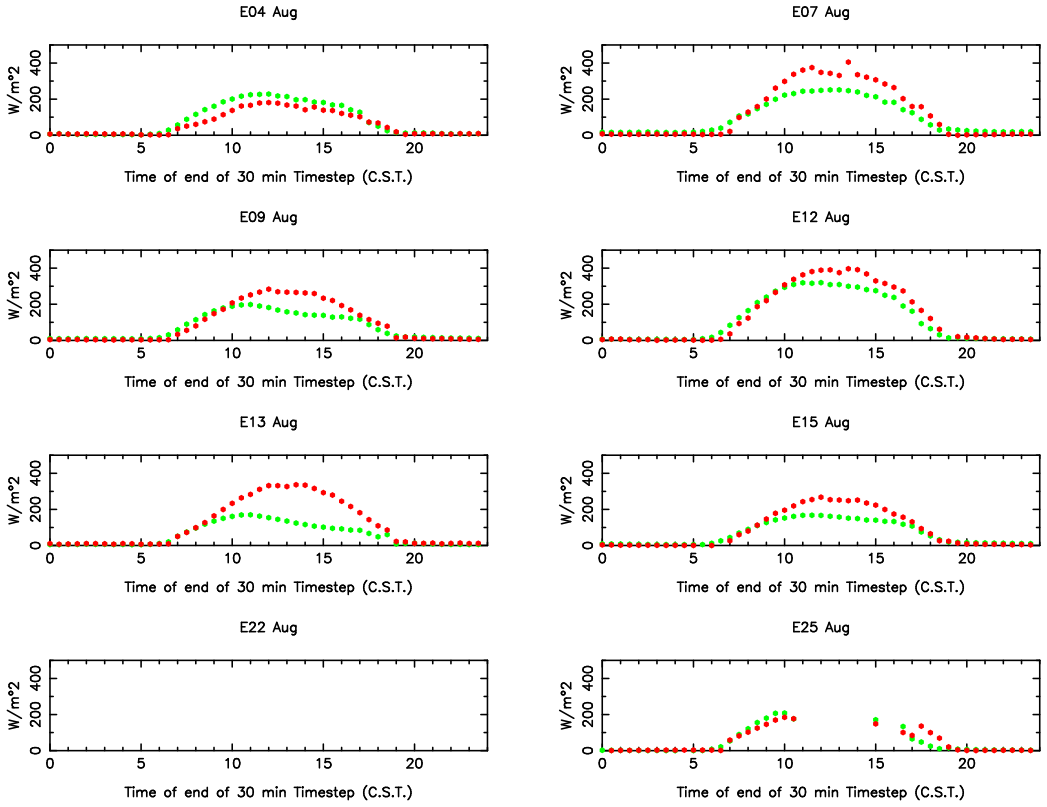

Figure 3.12: Mean latent flux 12AM-12AM CST diurnal cycle for August 2000, data red, model green.

Sensible Heat Flux

As with latent heat flux, sensible heat flux suffers from overestimation at night and underestimation of large positive values (Fig. 3.13). However, some exceptions include E15 which has a generally positive model bias, and E07 which has little bias at all. This difference is related to a competition between G and H. Sites with an extreme overestimation of downward daytime soil heat flux (see below) have the largest underestimation of upward daytime sensible heat flux, whereas sites like E07 and E15 have more reasonable G diurnal cycles. H is overestimated at E15 because LE is underestimated. At E04 and E25, on the other hand, G is actually rather well simulated, but H is too low in the late summer because the model is overestimating LE.

The observed seasonal cycle in daytime sensible heat varies from site to site. Some have substantial peaks in the spring and fall, while at other sites the seasonal cycle is weak (Fig. 3.14). These patterns are driven by net radiation and vegetation. Low net radiation causes low winter sensible flux, while active transpiration causes low summer sensible flux. When transpiration is low but radiation is high, $H + G$ must also be high, which means that $H + G$ is a bimodal function with peaks in the spring and fall. At a site like E12, H is dominant and strongly bimodal, while at E07 G and H share energy more evenly, so that peaks in H are muted. The model does not correctly capture these site-to-site differences, tending to underestimate the H seasonal cycle at most sites other than E07 and E15. Only at E07 and E15 does the model

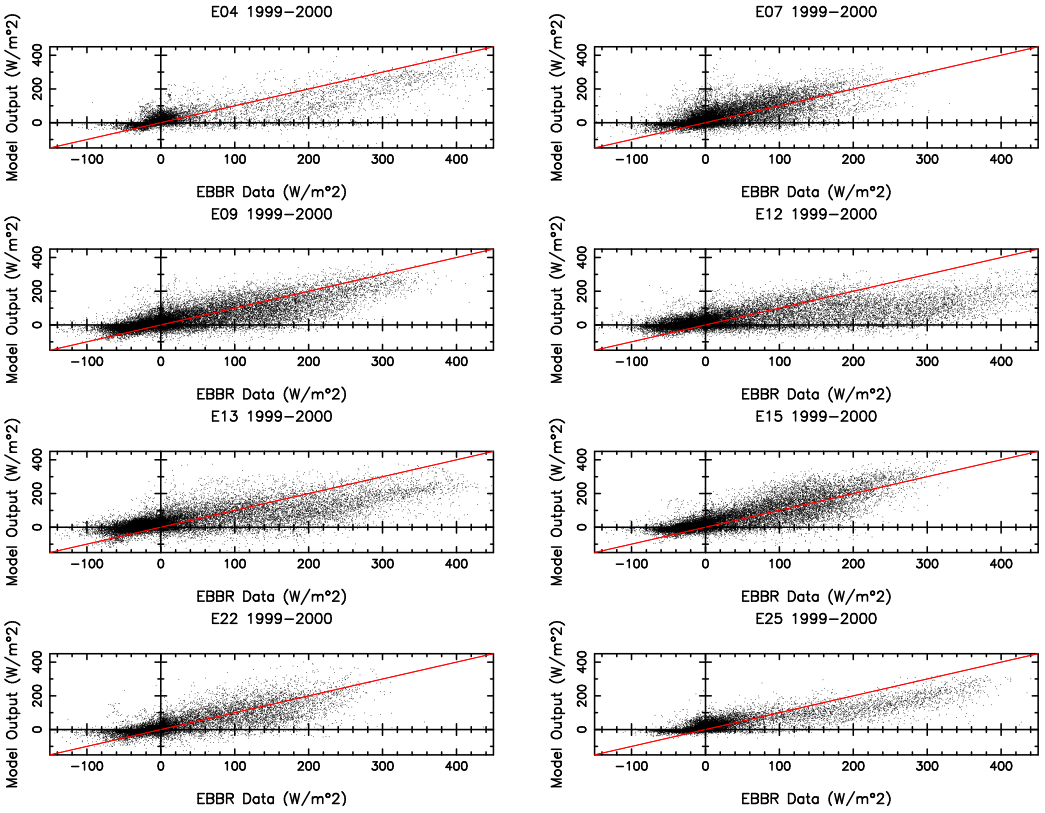

Figure 3.13: Half hourly SiB3 sensible heat flux versus observations

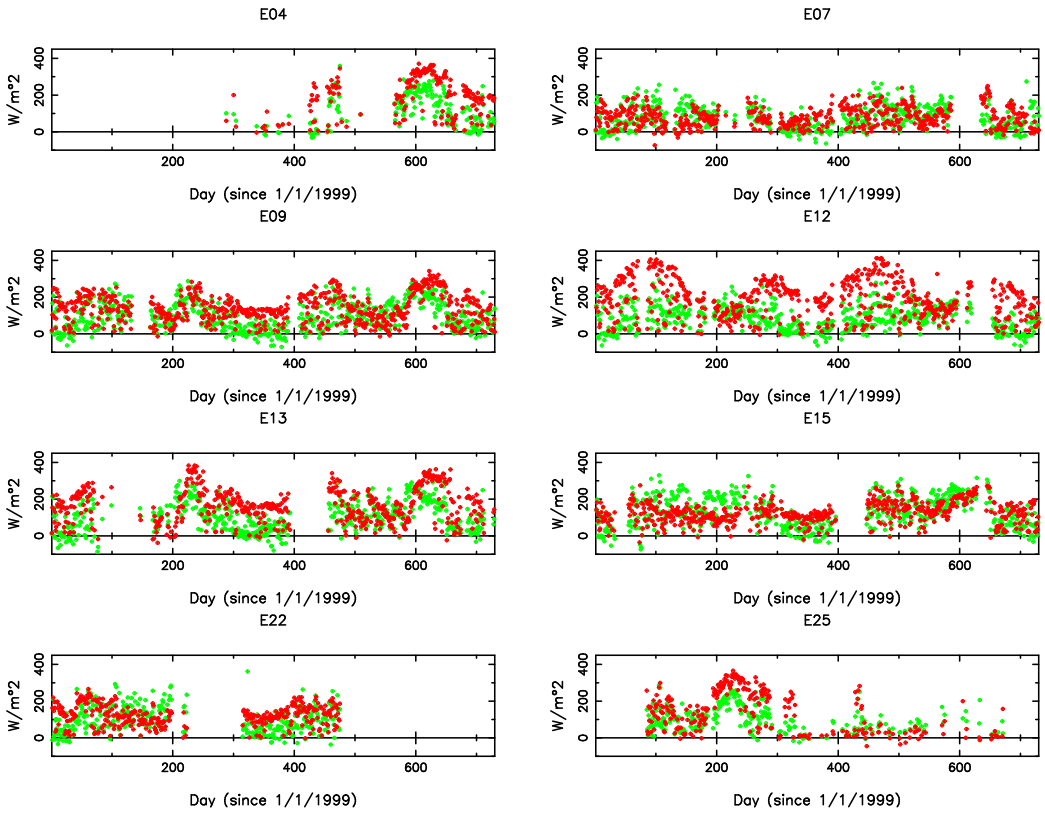

Figure 3.14: Daily mean 11-15 CST sensible heat fluxes for 1999-2000, with the EBBR data in red and the model output in green.

overestimate summer sensible heat flux the way it did at the AmeriFlux site. However, at E09 and E13, the sensible heat flux grows large too early in the late summer, consistent with the early drop off of latent flux.

The winter diurnal cycles are poorly simulated with sensible heat considerably underestimated and peaking several hours too early in the day (Fig. 3.15). The simulation is much worse at certain sites, particularly E09, E12, and E13. In the summer, the diurnal cycles of H are simulated much more successfuly (Fig. 3.16).

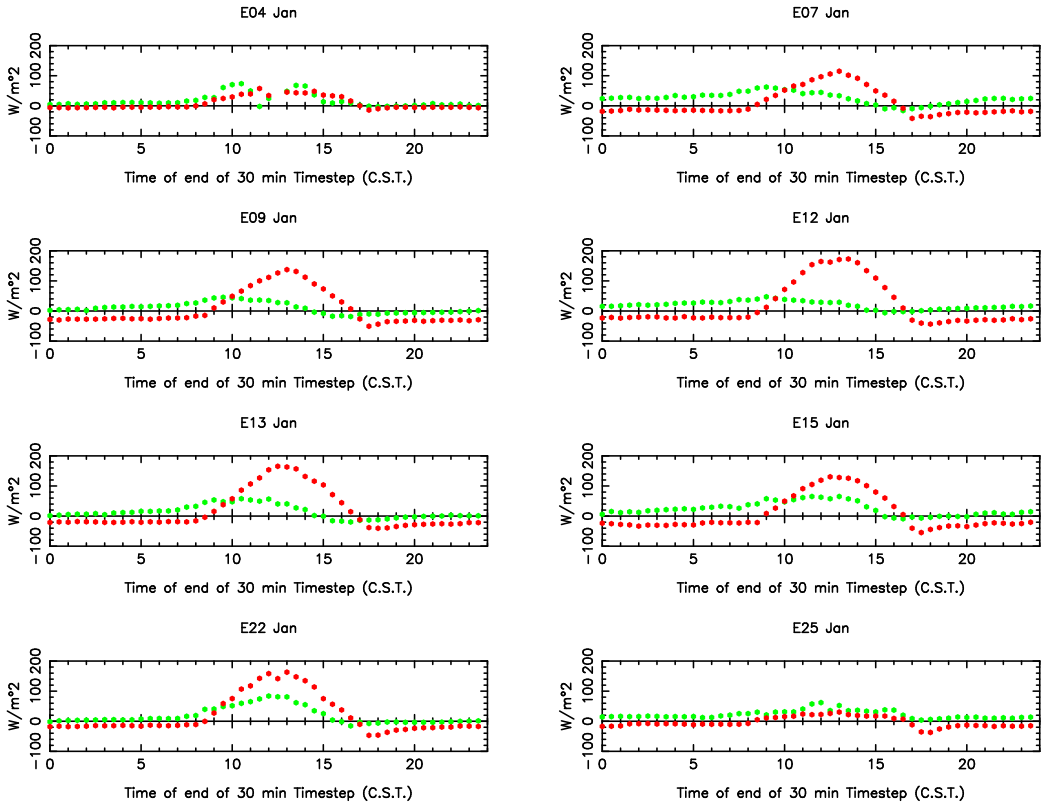

Figure 3.15: Mean sensible heat flux 12AM-12AM CST diurnal cycle for January 2000, data red, model green.

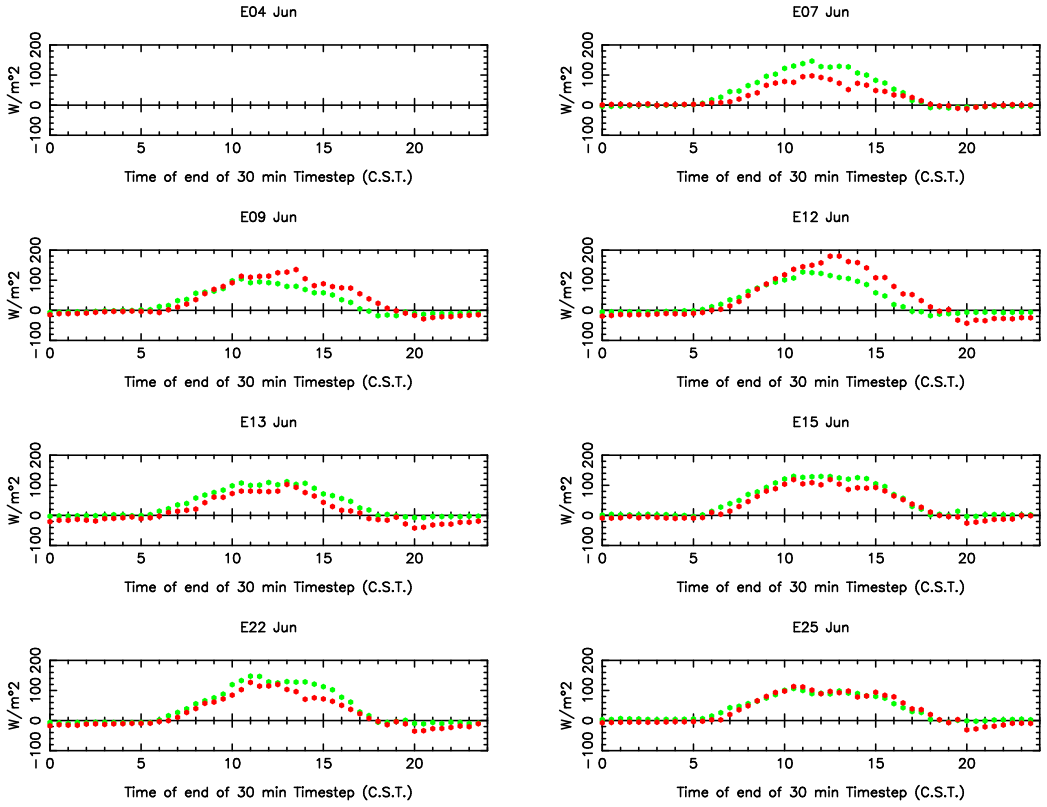

Figure 3.16: Mean sensible heat flux 12AM-12AM CST diurnal cycle for June 1999, data red, model green.

Ground Heat Flux

The model ground heat flux (G) has significantly too large a diurnal cycle, causing a large slope in simulation versus observation (Fig. 3.17). At E09, E12, and E13, this error ties in directly with the strong underestimation of the sensible heat diurnal cycle. However, at E04 and E25 it is evident that the errors in H are more related to errors in LE than in G, which is relatively well simulated.

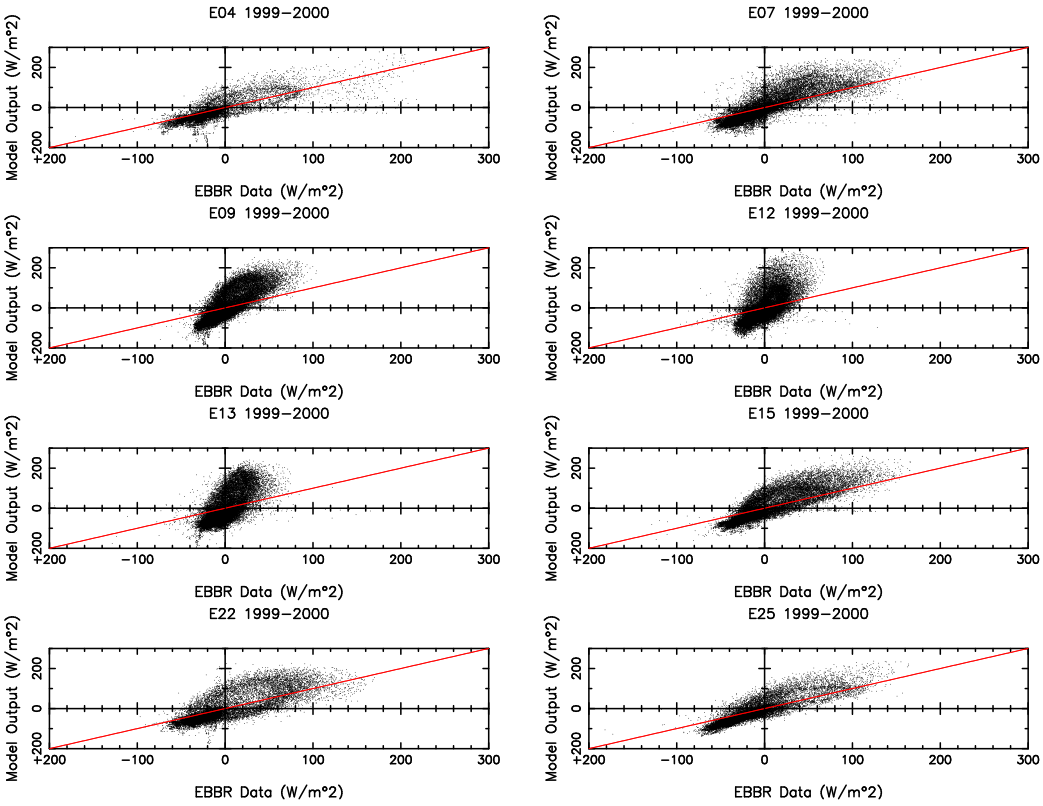

Figure 3.17: Half hourly SiB3 ground heat flux versus observations

There is too much daytime heat flux into the soil at all sites; primarily in

the dormant season at a few sites, but year round at several others (Fig. 3.18). At a few of the sites (E12,E13), the simulated ground heat flux is much more remeniscient of the measured sensible heat flux than the measured ground heat flux. A familiar theme: the model is allowing considerably too much soil heating, at the primary expense of turbulent sensible heat flux.

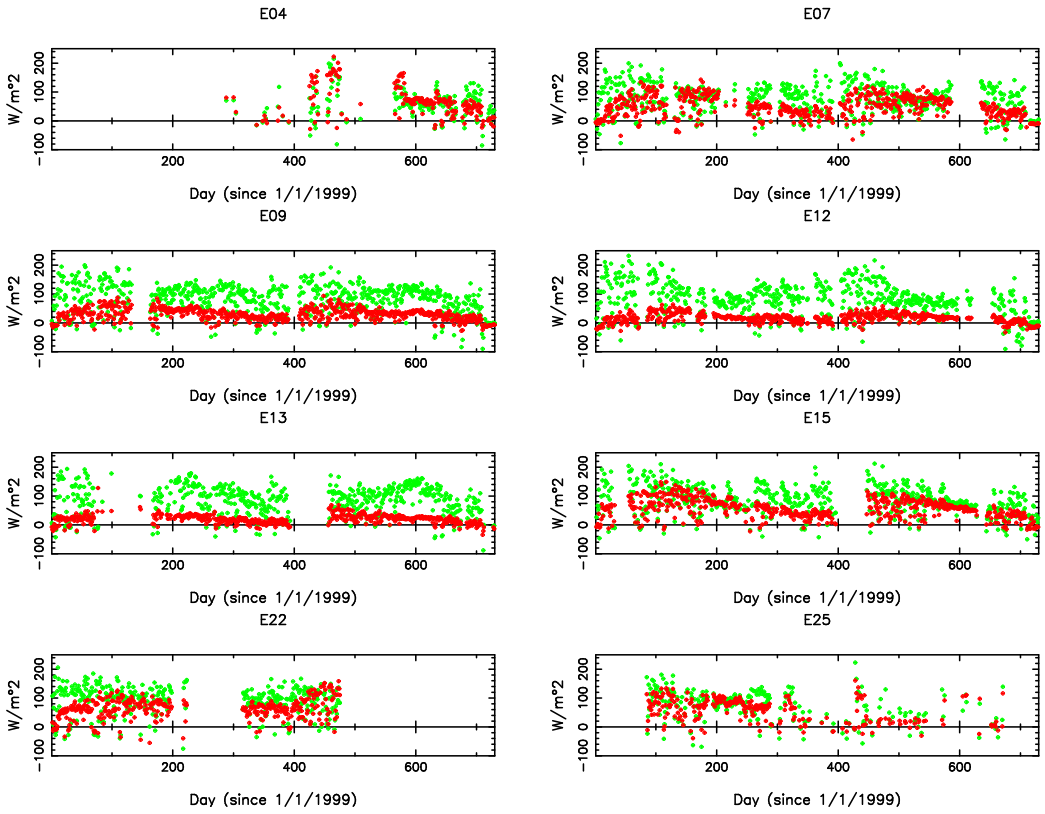

Figure 3.18: Daily mean 11-15 CST ground heat fluxes for 1999-2000, with the EBBR data in red and the model output in green.

The model also simulated too much heat emerging from the soil at night, year-round (Fig. 3.19). An example of the pathological diurnal cycle in ground heat flux is presented from August, 2000 (Fig. 3.20). In addition

to having too much energy flow, the timing of daytime maximum downward G is too early in the day. On a diurnal mean, the model conforms well with the observations year round (not shown), indicating that the excess out-flux at night and excess in-flux by day are of comparable magnitude.

Vegetation cover, including non-photosynthetic material, is expected to reduce daytime ground heat flux by shading (Yang et al 1999), so insufficient shading could contribute to excessive daytime soil heating. As at the AmeriFlux site, a test run was made to allow retention of dead leaves into the dormant season. In this case, the dead leaf area index formulation was modified to allow dead leaves to persist longer than one month. The results were similar: daytime ground heat flux was reduced somewhat, but remained too high (not shown).

Another potential cause for excessive ground heat flux is the soil itself; both the thermal conductivity and heat capacity of dry soil material and the amount of soil water (which affects soil thermal properties), may be improperly simulated.

Soils

ARM SWATS measurements were made hourly at various depths. While SiB3 node depths were not identical to SWATS depths, most SWATS depths were close enough to a SiB3 node to compare directly. For a few SWATS depths, the SiB3 results from the two levels on either side of the SWATS

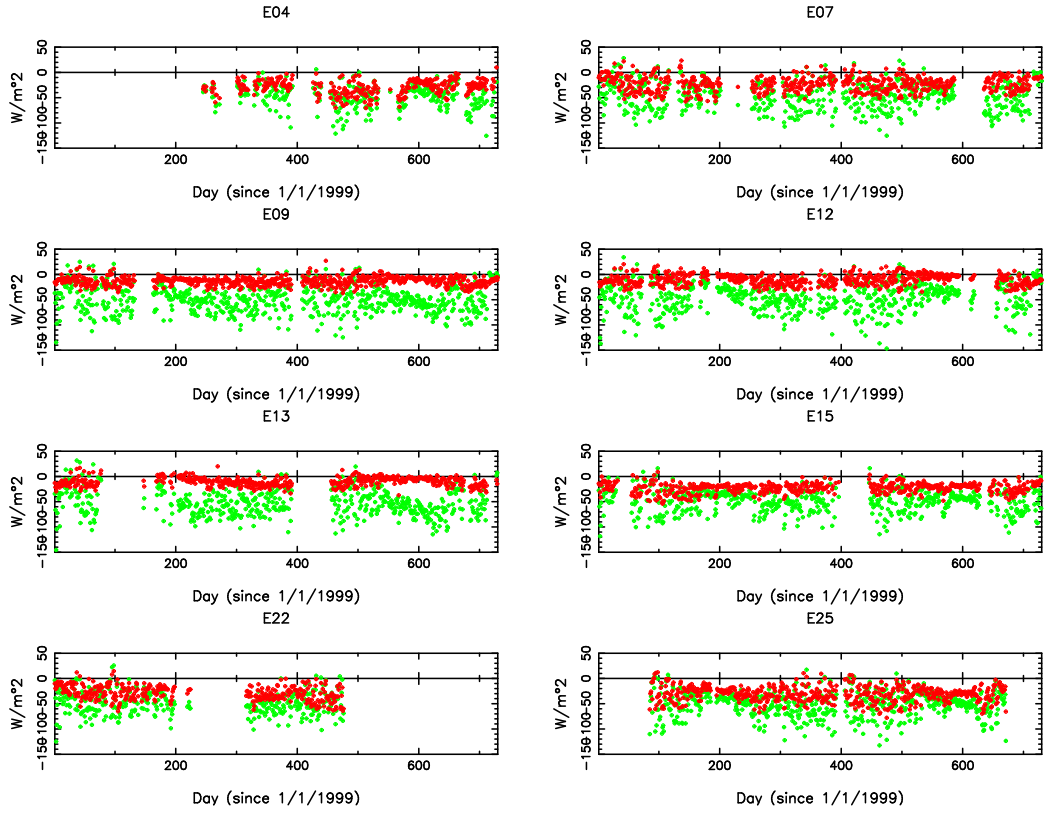

Figure 3.19: Daily mean 23-03 CST ground heat fluxes for 1999-2000, with the EBBR data in red and the model output in green.

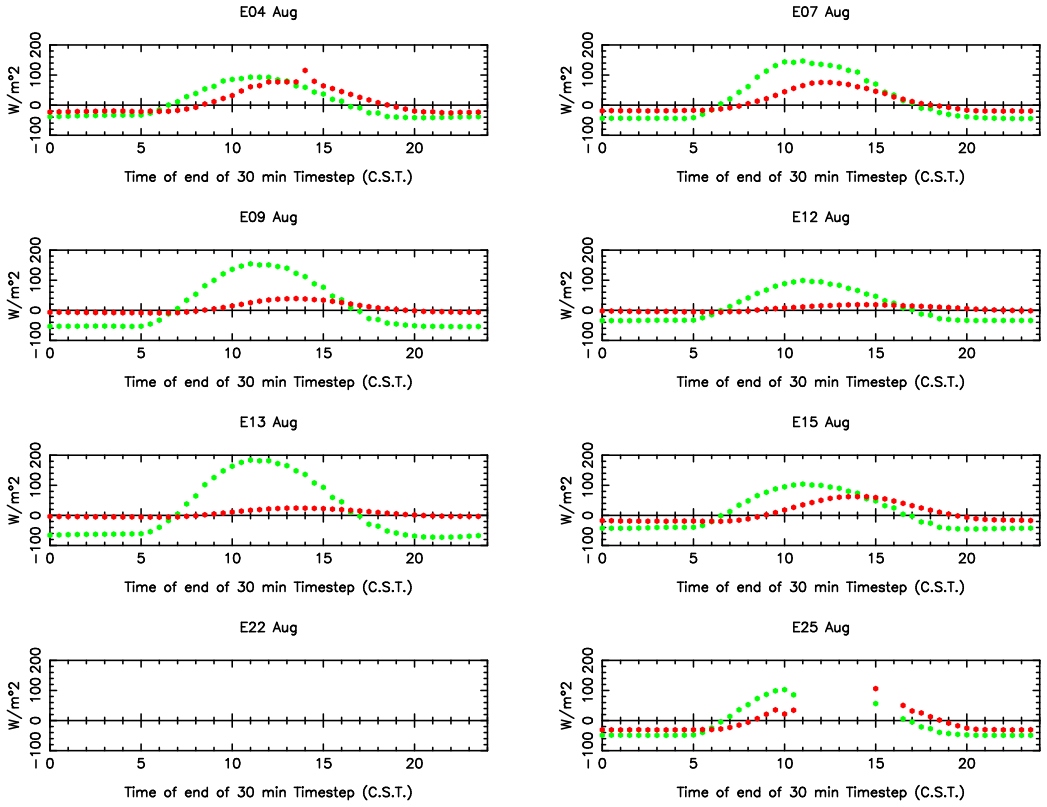

Figure 3.20: Mean ground heat flux 12AM-12AM CST diurnal cycle for August 2000, data red, model green.

depth were averaged.

The diurnal and seasonal cycles of soil temperature are larger in the simulations than in the observations, at all depths (Fig. 3.21, Fig. 3.22, Fig. 3.23). Sites at which ground heat flux was better simulated usually had better soil temperatures as well.

In the upper layers, soils tended to get too hot during the day in the summer, while the night temperatures were more reasonable. This is consistent with not enough vegetation shading, which would cause excessive daytime soil heating. At night, upward G is too high while soil temperatures adjust towards the air temperature, which stays close to the prescribed uppper boundary condition. However, particularly at depth, the winter soils are too cold, which cannot be explained by a lack of shading: soil parameters are also implicated.

Considering the limitations of the SWATS water observations, and the differences between the model and data soil retention curves, the soil water is well simulated by SiB3 (Fig. 3.24, Fig. 3.25). Particularly, the rates of drying in the summer are comparable. There are some key differeneces between the model and the data.

Hydraulic conductivity, like thermal conductivity, appears to be too high in the model, especially in the winter and spring where the data are less sensitive to precipitation events. However, SWATS hydraulic conductivity is underestimated in sandier soils, (E04, E12, E15, and E25), so the model is

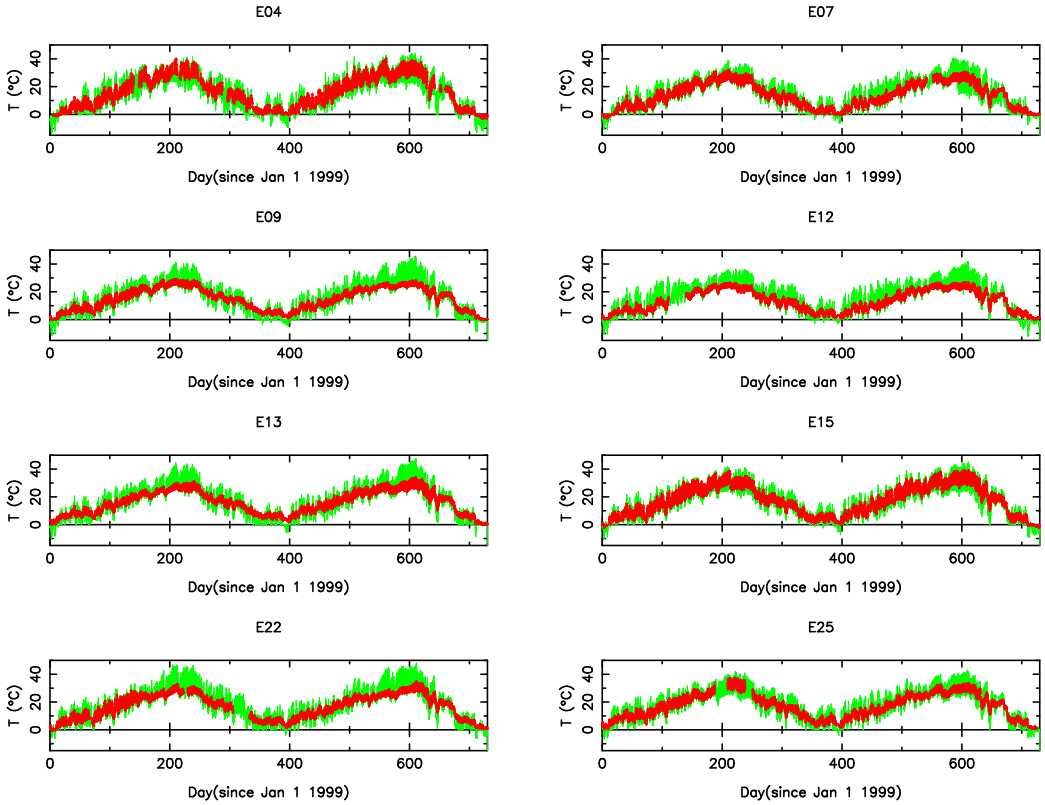

Figure 3.21: 1999-2000 soil temperature at 5 cm. SWATS data is red, SiB3 output is green.

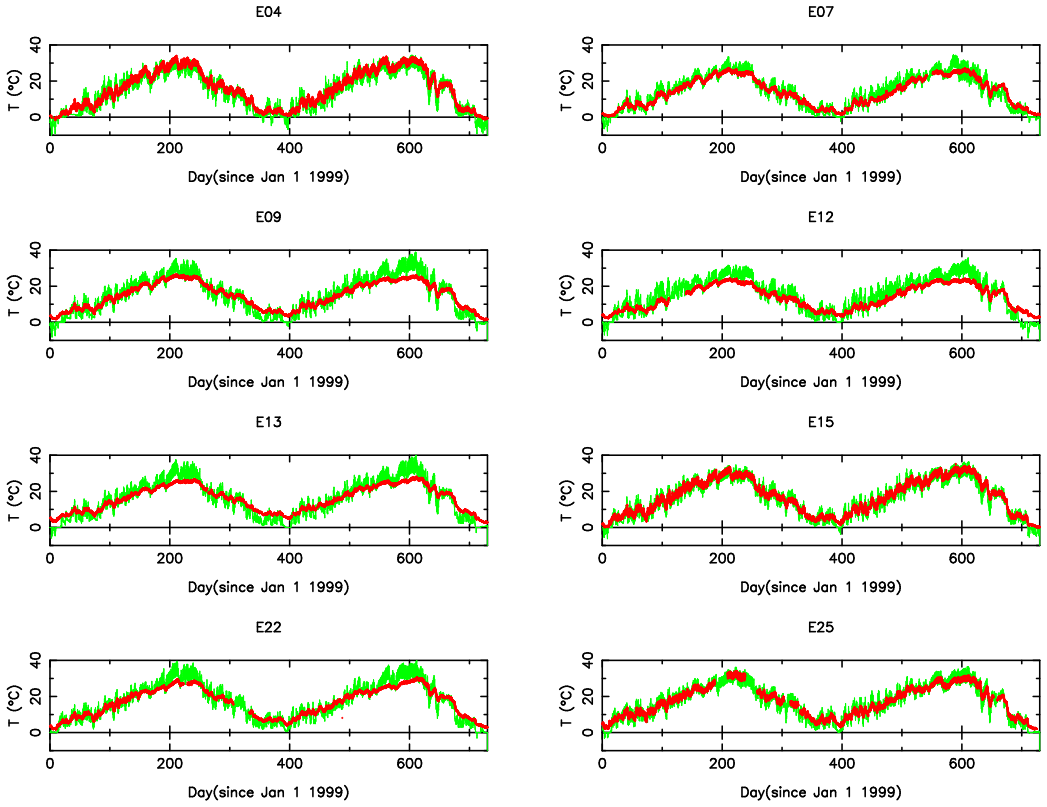

Figure 3.22: 1999-2000 soil temperature at 25 cm. SWATS data is red, SiB3 output is green.

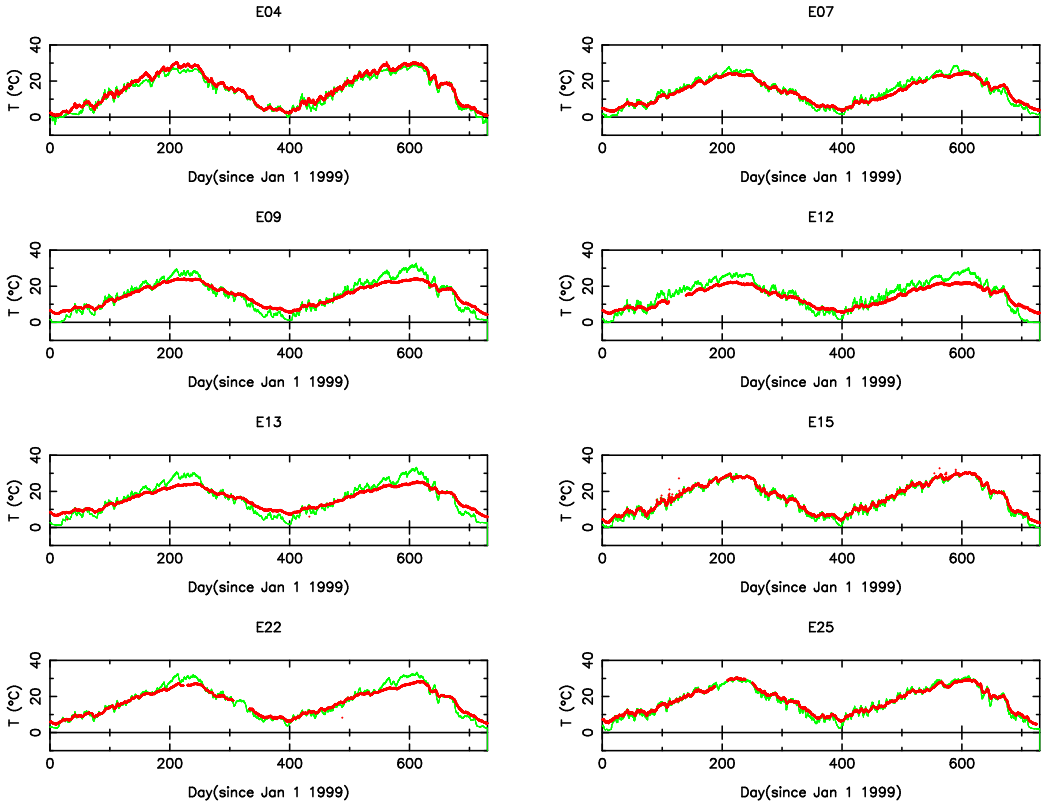

Figure 3.23: 1999-2000 soil temperature at 60 cm. SWATS data is red, SiB3 output is green.

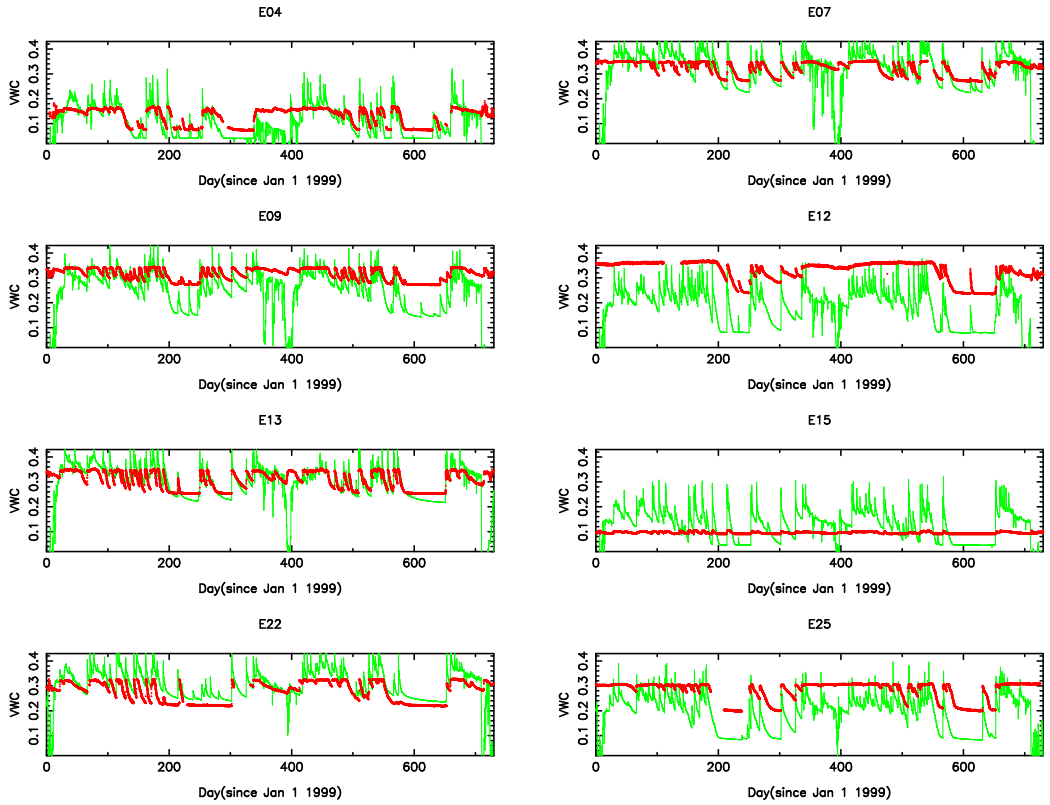

Figure 3.24: 1999-2000 soil volumetric water content at 5 cm. SWATS data is red, SiB3 output is green.

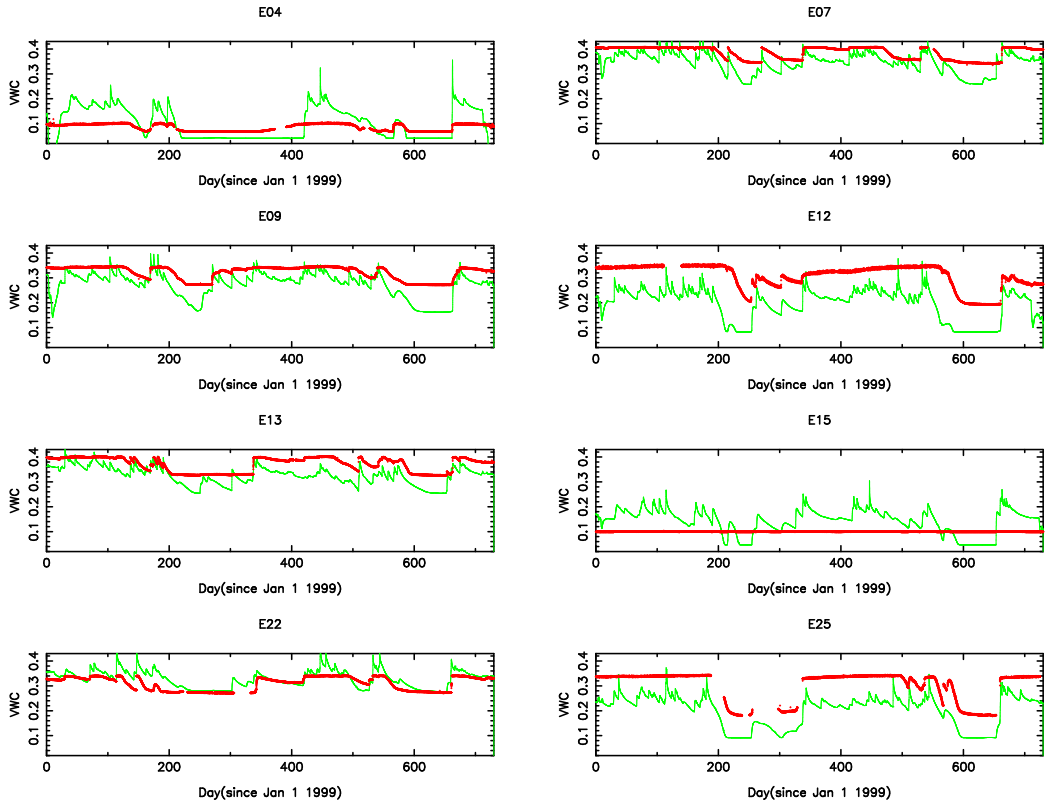

Figure 3.25: 1999-2000 soil volumetric water content at 35 cm. SWATS data is red, SiB3 output is green.

capturing the hyrdaulic conductivity better than it appears at these sites.

In the summer, SiB3 gets drier than the data at most of the sites. Part of this could be real, but also the SWATS data are expected to remain too high in dry soils, so again the model error is not as large as it appears. At E12 and E25, the model is considerably drier than the data year round. Part of this could be due to measurement error and the difference in SiB3 and SWATS retention curves, but the discrepancy seems too large to be entirely explained away. The clay that is often found in the deepest parts of the soil in Oklahoma (Hanan et al 2005) would be expected to yield wet upper layers because of the low hydraulic conductivity of clay (Campbell 1985). Therefore, a soil texture that varies with depth may improve these simulations.

Extreme drops in the modeled volumetric water content in the winter are soil freezing events; no comparison to data is possible at that time, because SWATS moisture data are not reliable in frozen soils (R. McCord, pers. comm.). Nonetheless, SiB3 probably does freeze too much considering that its soils get too cold in the winter.

There is no apparent correlation between the soil moisture model error and soil temperature model error, despite the fact that soil thermal conductivity is dependent on soil water. E07 and E13 both well simulate the water, but E07 model output much better matches soil temperature and ground heat flux data. Meanwhile, E12 and E25 model runs both underestimate the water content year round, but E25 simulates better soil temperature, and E25 outperforms E13 thermally.

3.2.2 Physiology and Stress

Stress factors for high and low temperature ($F_{s,HT}$, $F_{s,LT}$) and soil water ($F_{s,w}$) are applied within the C3 and C4 photosynthesis models. They range between zero and one, and each one's effect is to multiply the unstressed photosynthesis rate to convert it into a stressed rate. Therefore, the lower the stress factor, the higher the stress. In the summer, $F_{s,HT}$ was nearly always the most significant stress factor, passing comfortably below 0.3 at E09 and E13 in 2000, although only reaching down to 0.6 at E07 in 1999. Meanwhile, in the late summer, soil $F_{s,w}$ only reached below 0.75 at two sites, and for a rather brief period. Low temperature stress frequently reached very low levels in the winter, below 0.25.

Total temperature stress is the combination of low and high temperature stress. During the day, in the summer, total temperature stress is completely high temperature stress unless it is a very unusual day. Even though the C3 fraction was only 0.4 in June and 0.2 in August at most of the sites, decreasing the onset temperature of heat stress for C3 vegetation from 313.16 K to 308.16 K increased the full canopy temperature stress by at least 33% during hot spells in late July 1999 (Fig. 3.26). The effect on leaf surface relative humidity is seen in Figure 3.27, where increasing the heat stress lowered the humidity by decreasing stomatal conductance and latent heat flux (Fig. 3.28). Via the Ball-Berry equation, a decreased leaf surface humidity leads to further decreases in stomatal conductance and latent heat. This response is a mechanism by which water vapor feedback loops could be instigated when

the model is coupled to a GCM.

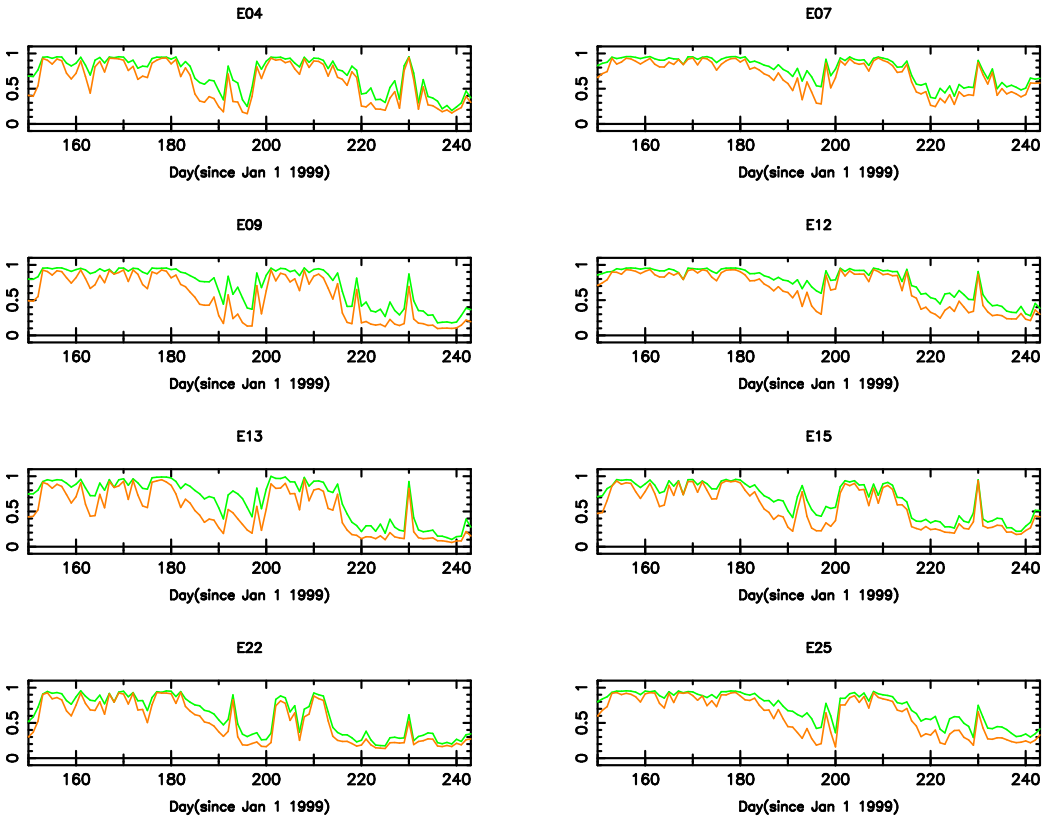

Figure 3.26: June - August 1999 daily mean 11-15 CST total temperature stress factor (mostly high temperature stress). The threshhold for high temperature stress in C3 plants is 308.16 K on the orange line, and 313.16 K on the green line. Values range from 0 to 1, with a **lower** value indicating **higher** stress.

In a second experiment, the pasture was assumed to be 100% C4 year round. In the mid and late summer, latent heat flux was slightly higher for full C4 than than with varying C4 fraction (Fig. 3.29). Therefore, the C4 photosynthetic pathway, with its prevention of Rubisco oxidation (photorespiration) and it's lower Ball-Berry slope parameter (greater water use

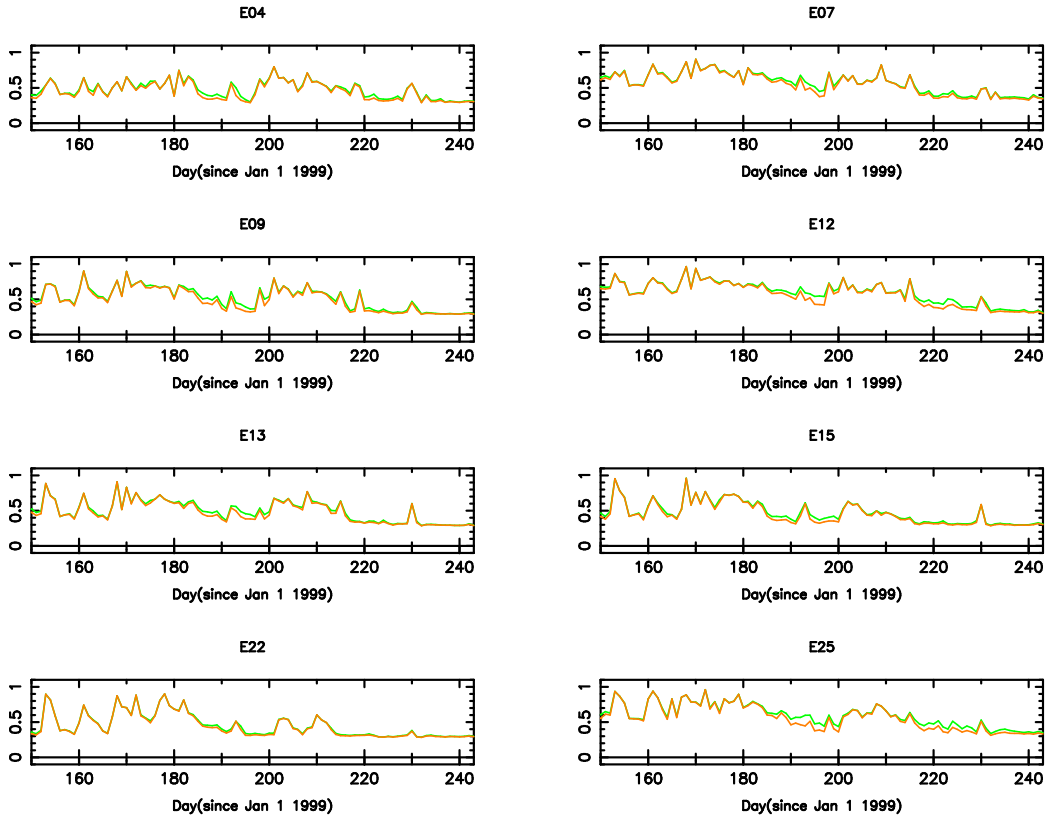

Figure 3.27: June - August 1999 daily mean 11-15 CST leaf surface relative humidity, with the C3 threshhold for heat stress being 308.16 K in the orange line and 313.16 K in the green line; in the latter, the C3 plants are more heat tolerant

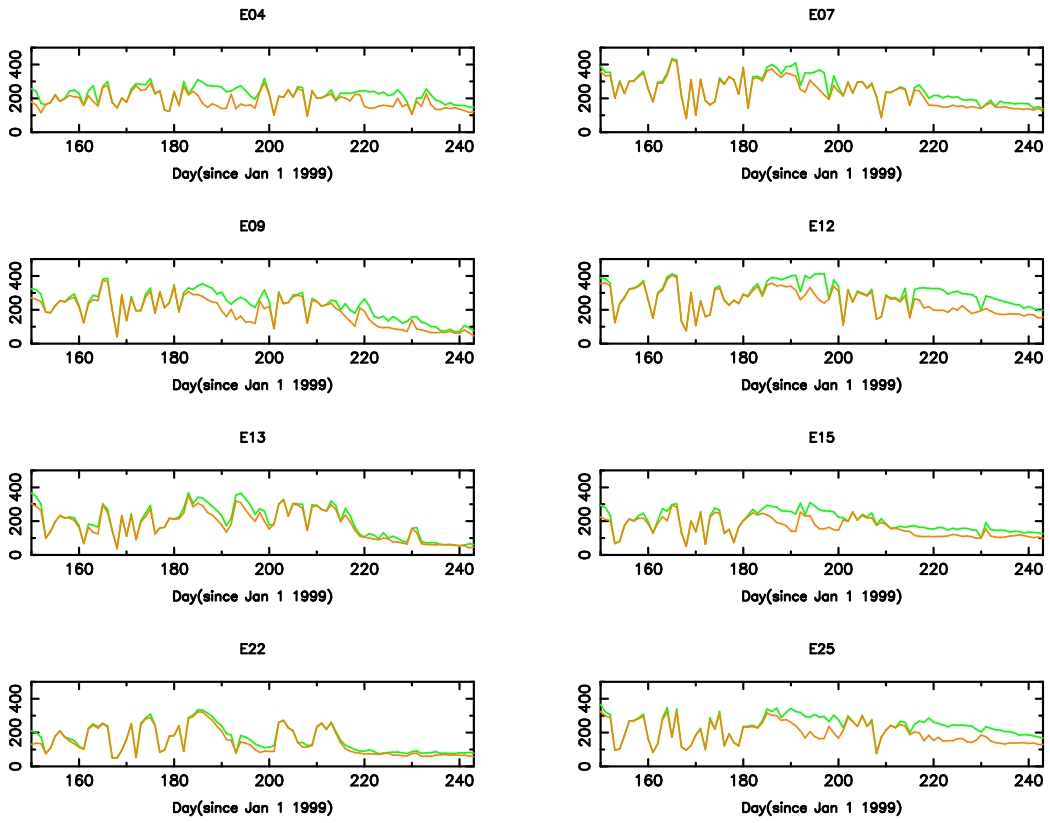

Figure 3.28: June - August 1999 daily mean 11-15 CST latent heat flux, with the threshhold parameter being 308.16 K in the orange line and 313.16 K in the green line; in the latter, the C3 plants are more heat tolerant

efficiency), is transpiring more in the heat of summer than C3, even though the C3 vegetation has the same high temperature stress threshhold. Carbon assimilation rates will be greater when latent flux is higher, so it makes sense that C4 grasses dominate the landscape in the late summer. However, in early summer the mixed canopy has just as much transpiration, and in spring it has more transpiration than the full C4 canopy. This could explain why Oklahoma grasslands have been observed to be half C3 and more than half C3 in the early summer and spring, respectively.

At most of the sites, the higher latent flux of the full C4 canopy of late summer is an improvement in model performance, but at E04 and E25 the mixed C3 and C4 canopy with the lower C3 stress threshhold performs the best of the three experiments. There is a large site to site difference in the way vegetation is responding to heat, which partly explains why the model errors in latent heat flux are so different from site to site.

3.2.3 NDVI Experiments

SiB3 runs using 1km SPOT and the 8km GIMMSg NDVI were compared. The derived $fPAR/k$ values were somewhat different between the two datasets (Fig. 3.30). Particularly at E15, the 8km pixels included more winter wheat, which has a peak $fPAR/k$ in the spring, a summer harvest, and a fall planting. The presence of wheat is also evident in the E13 data, at both resolutions. At a few of the sites, the different $fPAR/k$ values had a

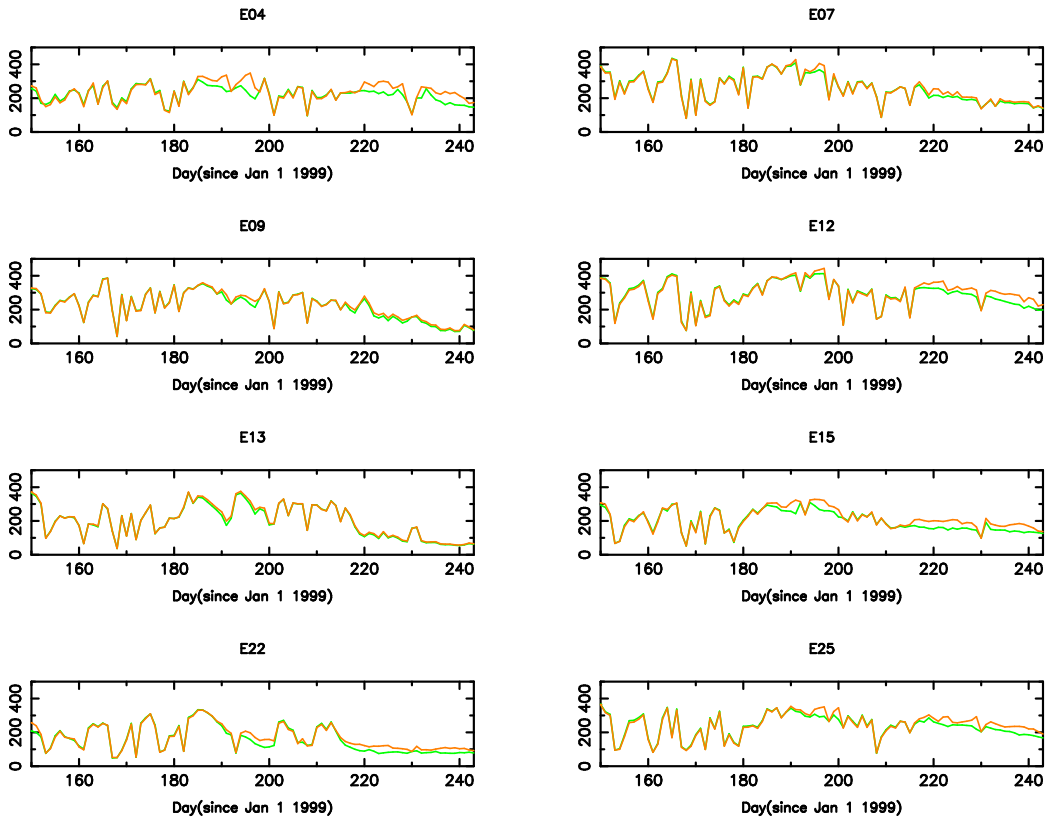

Figure 3.29: June - August 1999 daily mean 11-15 CST latent flux. The orange line indicates the flux when the pasture fraction is always completely C4, while the green line is the Standard run, using a time varying C4 fraction in the pasture.

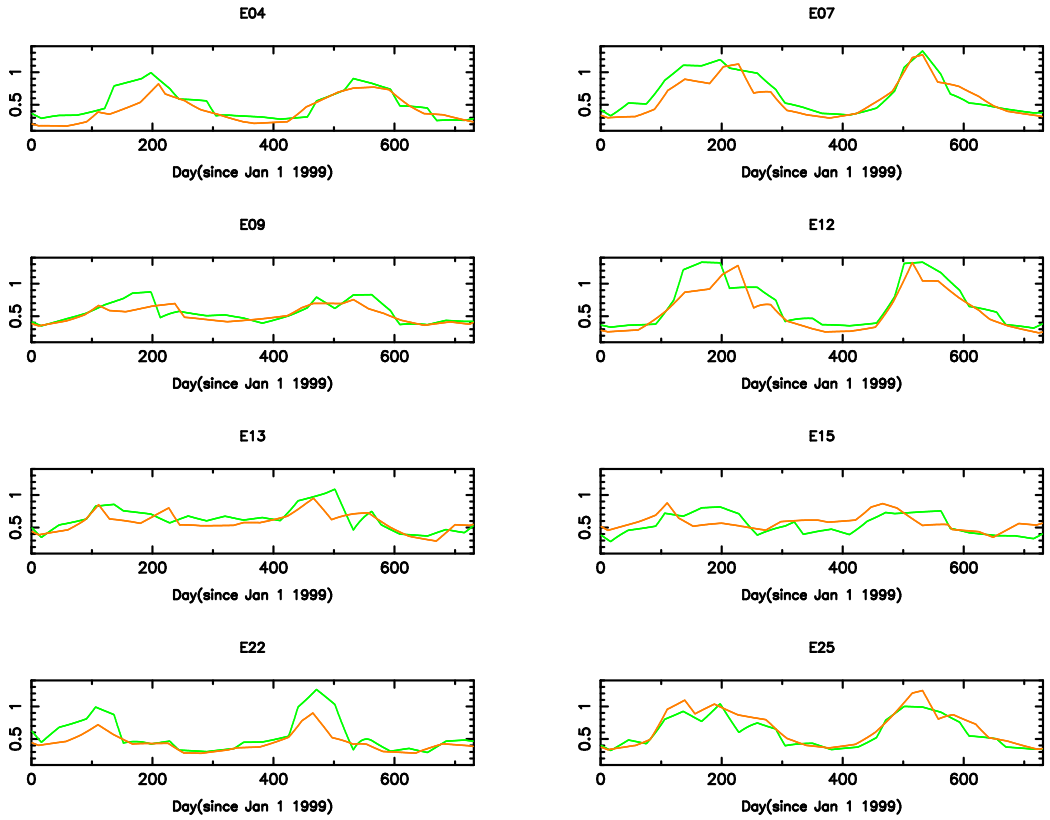

Figure 3.30: 1999-2000 fPAR/k canopy scaling parameter, using the GIMMSg 8km dataset (orange) and the SPOT 1km dataset (green)

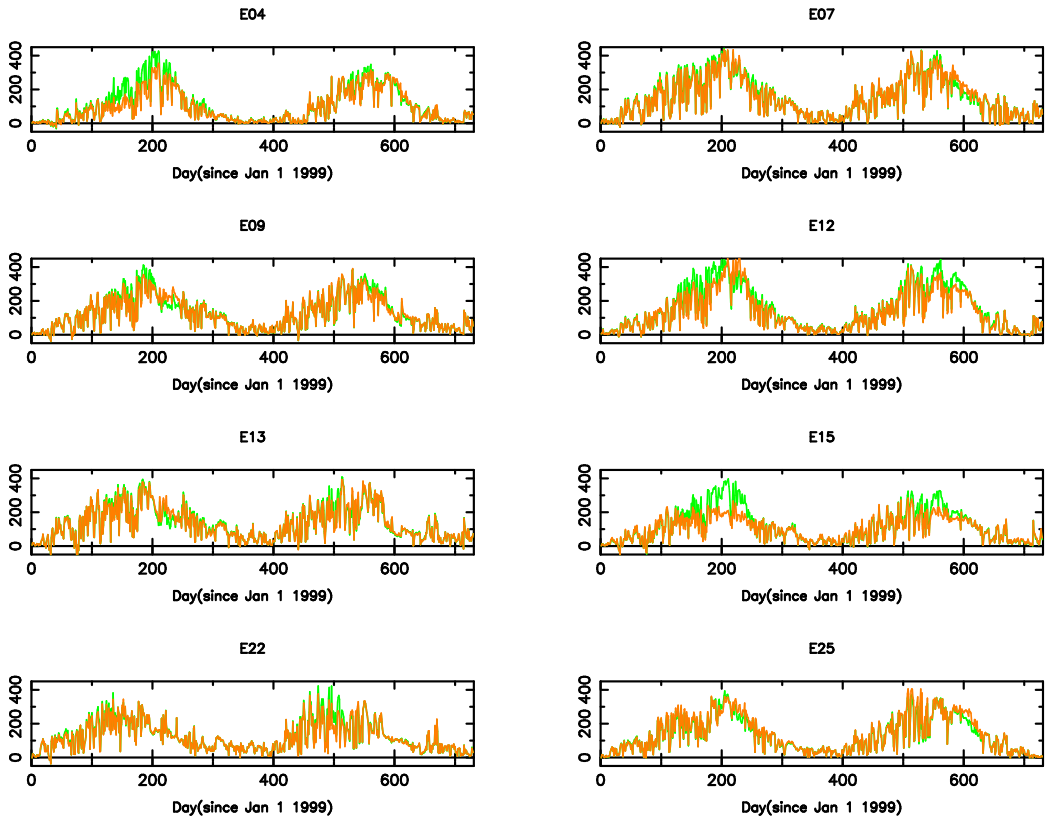

Figure 3.31: 1999-2000 11-15 CST daily mean latent heat fluxes from GIMMSg 8km satellite data (orange) and SPOT 1km data (green)

much larger effect on latent heat flux than at the AmeriFlux site (Fig. 3.31). Only at E15, however, was the use of SPOT consistently an improvement over GIMMSg in matching latent heat flux to the observations. In fact, at E12 in 1999, the GIMMSg dataset actually performed better than SPOT in having a late summer LE peak, though in 2000 SPOT performed better.

3.3 SiB3 coupled to the SCM

Stomatal suicide was not observed in the SiB3 - SCM simulation, whereas it was observed to drastically reduce late summer latent heat fluxes and canopy airspace water vapor in SiB2 - SCM.

Three runs involving the area averaged ARM-CART SiB3 parameter data: the Uncoupled run (SiB3 driven by ARM-E13 site data), the Prescribed SCM (SCM driven by observed fluxes), and the Coupled SCM (SCM driven by SiB3 fluxes) were compared to an old SiB2-SCM run (provided by Mark Branson, pers. comm.).

As evidenced by the canopy airspace water vapor (Fig. 3.32) and latent heat flux (Fig. 3.33), the SiB2-SCM system suffers from two periods of stomatal suicide: a brief period in mid July, and a longer period through most of August. These were eliminated by switching to SiB3. SiB3-SCM latent heat fluxes were somewhat higher than the observed fluxes, but considering that flux data are uncertain, the performance of SiB3-SCM is reasonable. Curiously, the Offline simulation had much higher water vapor contents than

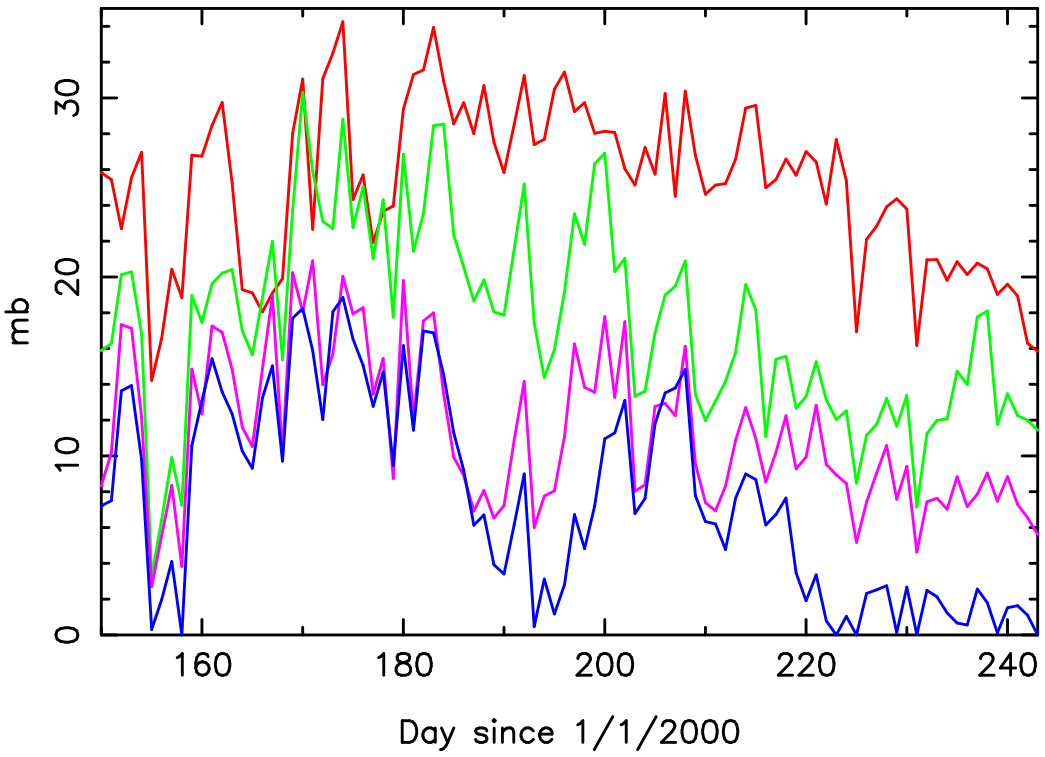

Figure 3.32: 2000 11-15 CST daily mean canopy airspace water vapor pressure: Offline SiB3 run (red), Prescribed Fluxes SCM (purple), Coupled SiB2-SCM (blue), and Coupled SiB3-SCM (green). The canopy airspace vapor pressure is linked aerodynamically to 2m ARM-E13 data in the Offline run, and to the middle of the PBL in the SCM runs.

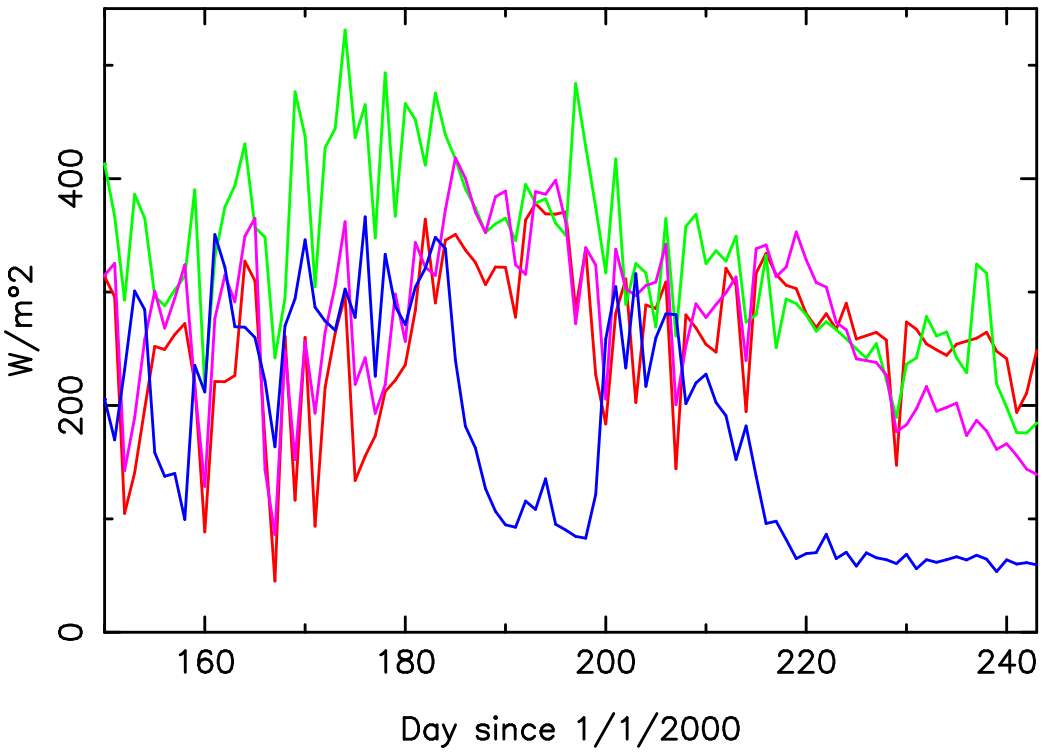

Figure 3.33: 2000 11-15 CST daily mean latent heat flux: Offline SiB3 Flux (red), Prescribed Flux (purple), Coupled SiB2-SCM Flux (blue), and Coupled SiB3-SCM Flux (green).

the SiB3-SCM runs despite having latent heat fluxes of a similar magnitude. It is likely that this is related to the use of a 2m water vapor observation in driving this model, as opposed to the PBL water vapor value that is used as the upper boundary condition of the SiB3-SCM. While the turbulence parameterization takes into account the 2m temperature observation height versus the mid-PBL height when coupled to the SCM, there appears to be some sort of error in these conversions in these particular simulations.

Annual precipitation for the year 2000 simulated by the SCM were 916 mm Prescribed and 1107 mm Coupled, which are good results considering that the eight ARM sites had between 760 and 1047 mm. SiB2-SCM yielded 930 mm in spite of stomatal suicide events, which is not less than the prescribed run because rain is not falling in any of the runs during the July and August dry spells. SiB2-SCM moisture recovers to acceptable values during rainy periods. The ARM E13 site only received 772 mm of precipitation in 2000, which is somewhat surprising for a centrally located site. However, the Offline SiB3 simulated latent heat flux did not seem to suffer from this lower rainfall, as it matched the domain-mean Prescribed flux well.

As suggested by Sud et al 2001, precipitation in ARM-CART SGP is controlled strongly by large scale atmospheric processes, with surface processes having a more intermittent effect. It was suggested that the surface fluxes have a larger effect on precipitation during wet and rainy periods than during dry or moderately wet periods. This is evident here as well, in the SiB2-SCM results as described above, but also in the SiB3-SCM results. SiB3-SCM has

higher latent heat flux than SiB2-SCM and the Prescribed run for nearly the entire summer. Therefore, during the wet periods when flux significantly impacts precipitation, the higher SiB3-SCM fluxes are responsible for the approximately 200 mm of extra rain produced by this run.

The fact that SiB3-SCM has somewhat more precipitation than the range seen in the eight ARM sites lends weight to the contention that this coupled model is running with too much latent heat flux. However, somewhat too wet of a simulation is far preferable in many applications to the SiB2-SCM stomatal suicide, which yields humidities in August that are extremely unrealistic for the SGP region.

Surface temperature (Fig. 3.34) and sensible heat flux (Fig. 3.35) showed that the SiB2-SCM stomatal suicide events, particularly the July event, corresponded to excessive heating of the air. SiB3-SCM is cooler than the other model runs in August, but otherwise there are only minor differences between the runs. The SiB3-SCM simulation of sensible heat is considerably better than SiB2-SCM. The Uncoupled SiB3 also performs well until late August, when it gets too low.

Overall, the SiB3-SCM is a significant improvement on the SiB2-SCM, and compares quite well with both the SCM driven by prescribed fluxes and the Offline SiB3 driven by ARM-E13 meteorology. Stomatal suicide was removed.

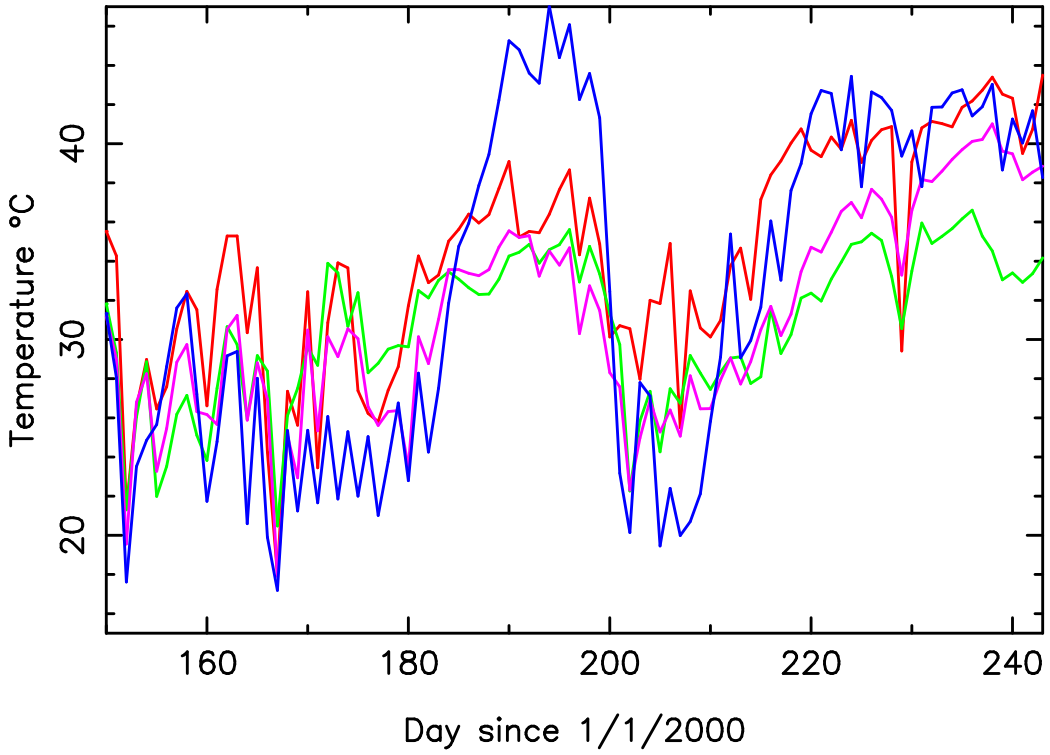

Figure 3.34: 2000 11-15 CST daily mean canopy airspace temperature: Offline SiB3 run (red), Prescribed Fluxes SCM (purple), Coupled SiB2-SCM (blue), and Coupled SiB3-SCM (green).

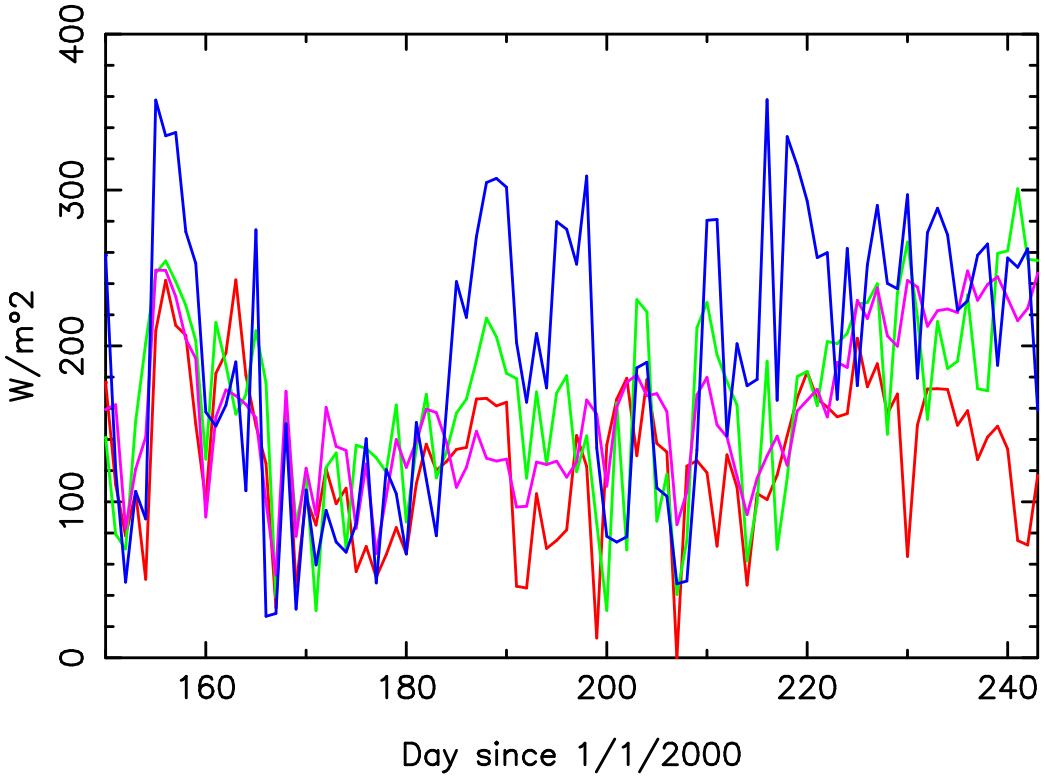

Figure 3.35: 2000 11-15 CST daily mean sensible heat flux: Offline SiB3 Flux (red), Prescribed Flux (purple), Coupled SiB2-SCM Flux (blue), and Coupled SiB3-SCM Flux (green).

Chapter 4

Conclusions

The Simple Biosphere Model version 3 (SiB3) does a reasonable job simulating the surface energy balance and water cycle at the ARM-CART SGP site, both when driven by observed weather and radiation, and when coupled to the CSU GCM in single column mode. Particularly, the partition between latent and sensible heat is well simulated, and the excessive stomatal dry air feedbacks have been reduced versus previous versions of coupled SiB-SCM systems.

4.1 Conclusions

Some key conclusions of this work include the following.

There was no stomatal suicide in SiB3 coupled to the CSU GCM Single Column Model at ARM-CART SGP. In fact, the SiB3 latent heat fluxes were

higher than observed, so that summer boundary layer water vapor mixing ratios and annual precipitation were higher using the SiB3-SCM than when using observed fluxes to drive the SCM. The ARM-CART SGP SCM simulation has been improved by replacing SiB2, which had stomatal suicide, with SiB3.

Using locally observed time invariant vegetation biophysical parameters and $fPAR$ and Leaf Area Index timeseries improved the simulation of carbon flux at a native prairie site over using standard parameters and satellite observations. Latent and sensible heat flux were less affected at this site. However, $fPAR$ had a greater impact on latent heat flux at some of the ARM sites. Also, the latent heat flux was increased at all of the ARM sites in the summer by increasing a single biophysical parameter: the threshhold temperature for heat stress of C3 vegetation. Latent heat flux was also increased by increasing the C4 fraction. At some sites, these two changes both improved the simulation, but at a few sites they increased the overestimation of latent heat flux. Therefore, there is a site to site variability in site characteristics that is not captured by these simulations.

Energy flow through the soil, and hence the diurnal and seasonal cycles in soil temperature, were overestimated by SiB3. However, from site to site, the magnitude of the error varied substantially. This error also affected latent and sensible heat fluxes, by causing their sum to be too small. During the night, this meant that downward latent and sensible flux were underestimated. During the day, the primary effect was to decrease upward sensible

heat flux. The problem was mitigated somewhat by increasing the retention of dead leaves, and hence increasing shading. However, the error was not eliminated by this attempt, and some of the problem must be related to errors in the thermal conductivity and heat capacity of the soil. One potential cause for this is errors in the soil water. However, soil water was simulated relatively well, and errors in soil water simulation could not be tied to errors in soil thermal behavior.

4.2 Future Work

Further modifications to SiB3 are nearing completion. Several improvements to the simulated carbon respiration have been tested. First, partitioning some of the respiration into a plant root and stem component proportional to $fPAR$ has yielded improvements at the AmeriFlux prairie sites as well as other temperate and boreal sites, and alternately an addition of a biogeochemical model to SiB3 to predict respiration has performed well at the sites (K. Schaefer, pers. comm.). Second, modifying the leaf to canopy photosynthesis scaling by adding a sun leaf and shade leaf model is also under testing (I.Baker, pers. comm.). Thirdly, the interpolation of NDVI based parameters between monthly values has been modified to delay the model's early onset of spring.

Further improvements suggested by this work include: investigating the methods of figuring leaf area index from NDVI data (to allow for better

treatment of grasslands), adding a soil texture that varies with depth, and investigating the formulation of soil heat capacities and conductivities (to try to understand why they are too high).

Data from within ARM-CART SGP will continue to be useful for SiB3 model development. Fluxes and SWATS data are still being collected, and some sites now report Eddy Correlation carbon fluxes now as well. There are approximately two dozen colocated flux and SWATS sites within the ARM network. Only 8 of these sites had dependable flux data for 1999-2000, but newer data can be trusted at all of the sites (D. Cook, pers. comm.). Meteorology and radiation data are available at all of these sites for creating filled datasets for running SiB3 in the uncoupled mode. Intensive field campaigns also continue to be performed in the region.

SiB3 produced reasonable simulations within the ARM-CART SGP region. Potential applications of SiB3, including coupling it to an atmospheric GCM to study climate and climate change, make it worthwile to further improve upon its performance. ARM-CART SGP provides a good testbed for these improvements.

REFERENCES

Baker, I., Denning, A.S., Hanan, N., Prihodko, L., Uliasz, M., Vidale, P.-L., Davis, K. and Bakwin, P. 2003. Simulated and observed fluxes of sensible and latent heat and CO2 at the WLEF-TV tower using SiB 2.5. *Global Change Biology*, 9:1262-1277.

Betts, A.K., J.H. Ball, A.C.M. Beljaars, M.J. Miller, and P.A. Viterbo. 1996. The land surface-atmosphere interaction: A review based on observational and global modeling perspectives. *Journal of Geophysical Research*, 101:7209-7225.

Bonan, G.B., 1996: A land surface model (LSM version 1.0) for ecological, hydrological, and atmospheric studies: Technical description and user's guide. NCAR Tech. NOte NCAR/TN-417+STR, 150 pp.

Brotzge, J.A. and K.C. Crawford. 2003. Examination of the surface energy budget: A comparison of Eddy Correlation and Bowen Ratio measurement systems. *Journal of Hydrometeorology*, 4:160-178.

Burba, G.G. and S.B. Verma. 2001. Prairie growth, PAR albedo and seasonal distribution of energy fluxes. *Agricultural and Forest Meteorology*, 107:227-240.

Campbell, G.S. 1985. *Soil physics with BASIC: transport models for soil-plant systems*. Amsterdam, New York : Elsevier.

Cassel, D.K. and D.R. Nielsen. 1986. Field capacity and available water capacity. In *Methods of Soil Analysis Part I Physical and Mineralogical Methods*, 2nd edition, ed. A. Klute, A., 901-926. Madison, WI: American Society of Agronomy.

Clapp, R.B. and G.M. Hornberger. 1978. Empirical equations for some soil hydraulic properties. *Water Resources Research*, 14:601-604.

Collatz, G.J., J.T. Ball, C. Grivet, and J.A. Berry. 1991. Physiological and environmental regulation of stomatal conductance, photosynthesis and transpiration: A model that includes a laminar boundary layer. *Agricultural and Forest Meteorology*, 54:107-136.

Collatz, G.J., M. Ribas-Carbo, and J.A. Berry. 1992. Coupled photosynthesis - stomatal conductance model for leaves of C4 Plants. *Australian Journal of Plant Physiology*, 19:519-538.

Collatz, G.J., J.A. Berry, and J.S. Clark. 1998. Effects of climate and atmosphereic CO2 partial pressure on the global distribution of C4 grasses: present, past, and future. *Oecologia*, 114:441-454.

Colello, G.D., C. Grivet, P.J. Sellers, and J.A. Berry. 1998. Modeling of energy, water, and CO2 flux in a temperate grassland ecosystem with SiB2: May-October 1987. *Journal of the Atmospheric Sciences*, 55:1141-1169.

Cook, D.R. 2005. "Energy Balance Bowen Ratio (EBBR) Handbook". Atmospheric Radiation Measurement Climate Research Facility. `http://www.arm.gov/instruments/instrument.php?id=ebbr`

Cosby, B.J., G.M. Hornberger, R.B. Clapp, and T.R. Ginn. 1984. A statistical exploration of the relationship of soil moisture characteristics to the physical properties of soils. *Water Resources Research*, 20:682-690.

Dai, Y., X. Zeng, R.E. Dickinson, I. Baker, G.B. Bonan, M.G. Bosilovich, A.S. Denning, P. Dirmeyer, P.R. Houser, G. Niu, K.W. Oleson, C.A. Schlosser, and Z.-L. Yang. 2003. The Common Land Model. *Bulletin of the American Meteorological Society*, 84:1013-1023.

Denning, A.S., G.J. Collatz, C. Zhang, D.A. Randall, J.A. Berry, P.J. Sellers, G.D. Colello, and D.A. Dazlich. 1996a. Simulations of terrestrial carbon metabolism and atmospheric CO2 in a general circulation model. Part1: Surface carbon fluxes. *Tellus*, 48B:521-542.

Denning, A.S, D.A. Randall, G.J. Collatz, and P.J. Sellers. 1996b. Simulations of terrestrial carbon metabolism and atmospheric CO2 in a general circulation model. Part 2: Simulated CO2 concentrations. *Tellus*, 48B:543-567.

Eltahir, E.A.B. 1998. A soil moisture-rainfall feedback mechanism 1. Theory and observations. *Water Resources Research*, 34:765-776.

Farquhar, G.D., S. von Caemmerer, and J.A. Berry. 1980. A biochemical model of photosynthetic CO2 assimilation in leaves of C3 plants. *Planta*, 149:78-90.

Field, R.T., L.J. Fritschen,E.T. Kanemasu, E.A. Smith, J.B. Stewart, S.B. Verma, and W.P. Kustas. 1992. Calibration, comparison, and correction of net radiation instruments used during FIFE. *Journal of Geophysical Research*, 97:18681-18695.

Fritschen, L.J. and J.R. Simpson. 1989. Surface energy and radiation balance systems: general description and improvement. *Journal of Applied Meteorology*, 28:680-689.

Fritschen, L.J. and P. Qian. 1992. Variation in energy balance components from six sites in a native prairie for three years. *Journal of Geophysical Research*, 97:18651-18661.

Fritschen, L.J., P. Qian, E.T. Kanemasu, D. Nie, E.A. Smith, J.B. Stewart, S.B. Verma, and M.L. Wesely. 1992. Comparisons of surface flux measurment systems used in FIFE 1989. *Journal of Geophysical Research*, 97:18697-18713.

Garratt, J.R. 1993. Sensitivity of climate simulations to land surface and atmospheric boundary-layer treatment-A review. *Journal of Climate*, 6:419-449.

Ghan, S.J., J.C. Liljegren, W.J. Shaw, J.H. Hubbe, and J.C. Doran. 1997. Influence of subgrid variability on surface hydrology. *Journal of Climate*, 10:3157-3166.

Hanan, N.P., J.A. Berry, S.B. Verma, E.A. Walter-Shea, A.E. Suyker, G.G. Burba, and A.S. Denning. 2005. Testing a model of CO2, water and energy exchange in Great Plains tallgrass prairie and wheat ecosystems. *Agricultural and Forest Meteorology*, 131:162-179.

Heilman, J.L., C.L. Britten, and C.M.U. Neale. 1989. Fetch requirements for Bowen Ratio measurements of latent and sensible heat fluxes. *Agricultural and Forest Meteorology*, 44:261-273.

Holben, B.N. 1986. Characteristics of maximum-value composite images from temporal AVHRR data. *International Journal of Remote Sensing*, 7:1417-1434.

Hopkins, W.G. 1999. *Introduction to Plant Physiology.* New York: John Wiley and Sons.

Liu, J.L. 2004. Investigation of ecosystem drought stress and its impacts on carbon exchange in tropical forests. Masters Thesis, Colorado State University, Fort Collins, CO.

Los, S.O., G.J. Collatz, P.J. Sellers, C.M. Malmström, N.H. Pollack, R.S. DeFries, L. Bounoua, M.T. Parris, C.J. Tucker, and D.A. Dazlich. 2000. A global 9-yr biophysical land surface dataset from NOAA AVHRR data. *Journal of Hydrometeorology*, 1:183-199.

McCord, R.A., Hargrove, W.W., Brandt, C.C., and Jager, H.I. 2004. "ARM Data Products for Carbon Cycle Research". Environmental Sciences Division, Oak Ridge National Laboratory. `http://www.archive.arm.gov/Carbon/`.

Nie, D., E.T. Kanemasu, L.J. Fritschen, H.L. Weaver, E.A. Smith, S.B. Verma, R.T. Field, W.P. Kustas, and J.B. Stewart. 1992. An intercomparison of surface energy flux measurement systems used during FIFE 1987. *Journal of Geophysical Research*, 97:18715-18724.

Pinzon, J.E. 2002. Using HHT to successfully uncouple seasonal and interannual components in remotely sensed data. Paper presented at SCI International 2002 Conference Proceedings Jul 14-18, Orlando, Florida.

Pinzon, J.E., M.E. Brown, and C.J. Tucker. 2005. Satellite time series correction of orbital drift artifacts using empirical mode decomposition. In *Hilbert-Huang Transform: Introduction and Applications*, ed. Huang, N, 167-186.

Randall, D.A., D.A. Dazlich, C. Zhang, A.S. Denning, P.J. Sellers, C.J. Tucker, L. Bounoua, J.A. Berry, G.J. Collatz, C.B. Field, S.O. Los, C.O. Justice, and I. Fung. 1996. A revised land surface parameterization (SiB2) for GCMs. Part III: The greening of the Colorado State University General Circulation Model. *Journal of Climate*, 9:738-763.

Randall, D.A. and D.G. Cripe. 1999. Alternative methods for specification of observed forcing in single-column models and cloud system models. *Journal of Geophysical Research*, 104:24527-24545.

Reece, C.F. 1996. Evaluation of a line heat dissipation sensor for measuring soil matric potential. *Soil Science Society of America Journal*, 60:1022-1028.

Saint, G. 1995. SPOT-4 Vegetation system - association with high-resolution data for multiscale studies. *Advances in Spece Research*, 17:107-110.

Schneider, J.M., D.K. Fisher, R.L. Elliot, G.O. Brown, and C.P. Bahrmann. 2003. Spatiotemporal variations in soil water: First results from the ARM SGP CART Network. *Journal of Hydrometeorology*, 4:106-120.

Sellers, P.J., J.A. Berry, G.J. Collatz, C.B. Field, and F.G. Hall. 1992a. Canopy reflectance, photosynthesis and transpiration, III, A reanalysis using enzyme kinetics - Electron transport models of leaf physiology. *Remote Sensing of the Environment*, 42:187-216.

Sellers, P.J., M.D. Heiser, and F.G. Hall. 1992b. Relations between surface conductance and spectral vegetation indeces at intermediate (100 m2 to 15 km2) length scales. *Journal of Geophysical Research*, 97:19033-19059.

Sellers, P.J., F.G. Hall, G. Asrar, D.E. Strebel and R.E. Murphy. 1992c. An overview of the First ISLSCP Field Experiment. *Journal of Geophysical Research*, 97:18345-18372.

Sellers, P.J., D.A. Randall,G.J. Collatz, J.A. Berry, C.B. Field, D.A. Dazlich, C. Zhang, G.D. Colello, and L. Bounoua. 1996a. A revised land surface parameterization (SiB2) for atmospheric GCMs. Part I: Model formulation. *Journal of Climate*, 9:676-705.

Sellers, P.J., S.O. Los, C.J. Tucker, C.O. Justice, D.A. Dazlich, G.J. Collatz, and D.A. Randall. 1996b. A revised land surface parameterization (SiB2) for atmospheric GCMs. Part II: The generation of global fields of terrestrial biophysical parameters from satellite data. *Journal of Climate*, 9:706-737.

Sellers, P.J., R.E. Dickinson, D.A. Randall, A.K. Betts, F.G. Hall, J.A. Berry, G.J. Collatz, A.S. Denning, H.A. Mooney, C.A. Nobre, N. Sato, C.B. Field, and A. Henderson-Sellers. 1997. Modeling the exchnages of energy, water, and carbon between continents and the atmosphere. *Science*, 275:502-509.

Smith, E.A., A.Y. Hsu, W.L. Crossou, R.T. Field, L.J. Fritschen, R.J. Gurney, E.T. Kanemasu, W.P. Kustas, D. Nie, W.J. Shuttleworth, J.B. Stewart, S.B. Verma, H.L. Weaver, and M.L. Wesley. 1992. Area-averaged surface fluxes and their time-space variability over the FIFE experimental domain. *Journal of Geophysical Research*, 97:18599-18622.

Stainforth, D.A., T. Aina, C. Christensen, M. Collins,N. Faull, D.J. Frame, J.A. Kettelborough, S. Knight, A. Martin, J.M. Murphy, C. Piani, D. Sexton, L.A. Smith, R.A. Spicer, A.J. Thorpe, and M.R. Allen. 2005. Uncertainty in predictions of the climate response to rising levels of greenhouse gases. *Nature*, 433:403-406.

Stewart, J.B. and S.B. Verma. 1992. Comparison of surface fluxes and conductances at two contrasting sites within the FIFE area. *Journal of Geophysical Research*, 97:18623-18628.

Still, C.J., J.A. Berry, G.J. Collatz, and R.S. DeFries. 2003. Global distribution of C3 and C4 vegetation: carbon cycle implications. *Global Biogeochemical Cycles*, 17(1):1006, doi:10.1029/2001GB001807.

Stokes, G.M. and S.E. Schwartz. 1994. The Atmospheric Radiation Measurement (ARM) Program: Programmatic background and design of the Cloud and Radiation Test Bed. *Bulletin of the American Meteorological Society*, 75:1201-1221.

Sud, Y.C., D.M. Mocko, G.K. Walker, and R.D. Koster. 2001. Influence of land surface fluxes on precipitation: Inferences from simulations forced with four ARM-CART SCM datasets. *Journal of Climate*, 14:3666-3691.

Suyker, A.E. and S.B. Verma. 2001. Year-round observations of the net ecosystem exchange of carbon dioxide in a native tallgrass prairie. *Global Change Biology*, 7:279-289.

Suyker, A.E., S.B. Verma, and G.G. Burba. 2003. Interannual variability in net CO2 exchange of a native tallgrass prairie. *Global Change Biology*, 9:255-265.

Tucker, C.J., M.E. Brown, J.E. Pinzon, D.A. Slayback, R. Mahoney, N. El Saleous, and E.F. Vermote. 2005. An extended AVHRR 8-km NDVI dataset comparable with MODIS and SPOT Vegetation NDVI data. *International Journal of Remote Sensing*, 26:4485-4498.

Twine, T.E., W.P. Kustas, J.M. Norman, D.R. Cook, P.R. Houser, T.P. Meyers, J.H. Prueger, P.J. Starks, P.J., and M.L. Wesely. 2000. Correcting eddy-covariance flux underestimates over a grassland. *Agricultural and Forest Meteorology*, 103:279-300.

van Genuchten, M.Th. 1980. A closed form equation for predicting the hydraulic conductivity of unsaturated soils. *Soil Science Society of America Journal*, 44:892-898.

Verma, S.B., J. Kim, and R.J. Clement. 1992. Momentum, water vapor, and carbon dioxide exchange at a centrally located prairie site during FIFE. *Journal of Geophysical Research*, 97:18629-18639.

Villalobos, F.J. and E. Fereres. 1990. Evaporation measurements beneath corn, cotton, and sunflower canopies. *Agronomy Journal*, 82:1153-1159.

Yang, Z-L., Y. Dai, R.E. Dickinson, and W.J. Shuttleworth. 1999. Sensitivity of ground heat flux to vegetation cover fraction and leaf area index. *Journal of Geophysical Research*, 104:19505-19514.

Zeng, X., M. Shaikh, Y. Dai, R.E. Dickinson, and R. Myneni. 2002. Coupling of the Common Land Model to the NCAR Community Climate Model. *Journal of Climate*, 15:1832-1854.